

CHAPTER 5

vorgelegt von
Diplom-Physiker
Anton Haase
geboren in Berlin

Von der Fakultät II - Mathematik und Naturwissenschaften
der Technischen Universität Berlin
zur Erlangung des akademischen Grades
Doktor der Naturwissenschaften
Dr. rer. nat.

genehmigte Dissertation

Promotionsausschuss:

Vorsitzender: Prof. Dr. Mister Unbekannt
Gutachter: Prof. Dr. Stefan Eisebitt
Gutachter: Prof. Dr. Mathias Richter
Gutachterin: Dr. Saša Bajt

Tag der wissenschaftlichen Aussprache:

Berlin 2017

Contents

| | |
|---|-----------|
| 1 Introduction | 1 |
| 2 Theoretical Description of EUV and X-ray Scattering | 5 |
| 2.1 EUV and X-ray Radiation | 5 |
| 2.2 Interaction of EUV and X-ray Radiation With Matter | 6 |
| 2.2.1 Elastic Scattering | 9 |
| 2.2.2 Absorption and Fluorescence | 11 |
| 2.3 Specular Reflection from Surfaces and Interfaces in Layered Systems | 12 |
| 2.4 Diffuse Scattering in Layered Systems | 15 |
| 2.5 Grazing-incidence X-ray Fluorescence | 22 |
| 3 Experimental Setup and Sample Systems | 27 |
| 3.1 Synchrotron Radiation | 27 |
| 3.2 The Instrumentation for the EUV Spectral Range | 31 |
| 3.2.1 The EUV Beamlines at BESSYII and MLS | 31 |
| 3.2.2 The Experimental Endstations at the EUVR and SX700 Beamlines | 33 |
| 3.3 Grazing-incidence X-ray Fluorescence at the FCM Beamline | 36 |
| 3.4 Sample systems | 37 |
| 3.4.1 Choice of the Chemical Species and Multilayer Design | 38 |
| 3.4.2 Multilayer Deposition by Magnetron Sputtering | 39 |
| 4 Characterization of the Multilayer Structure for Different Systems | 41 |
| 4.1 Reconstruction Based on Specular EUV reflectance | 42 |
| 4.1.1 Multilayer Model and Particle Swarm Optimization | 44 |
| 4.1.2 Model Uniqueness and Maximum Likelihood Estimation | 47 |
| 4.2 Molybdenum Thickness Variation in Mo/Si/C Multilayers | 51 |
| 4.2.1 Sample systems and experimental procedure | 52 |
| 4.2.2 Combined Analysis of X-ray and EUV reflectance | 54 |
| 4.2.3 Optimization results | 59 |
| 4.3 Analysis of Cr/Sc Multilayers with Sub-nanometer Layer Thickness | 62 |
| 4.3.1 Reconstruction with a discrete layer model approach | 63 |

Contents

| | | |
|-------------------|--|------------|
| 4.3.2 | Extending The Model to Graded Interfaces and Interdiffusion | 67 |
| 4.3.3 | Addition of Complementary Experimental Methods | 71 |
| 4.3.4 | Reconstruction and Maximum Likelihood Evaluation | 74 |
| 5 | Analysis of Interface Roughness based on Diffuse Scattering | 83 |
| 5.1 | Near-normal Incidence Diffuse Scattering | 84 |
| 5.1.1 | Mapping Reciprocal Space for the Mo/B ₄ C/Si/C Sample | 87 |
| 5.1.2 | Kiessig-like Peaks and Resonant Effects | 89 |
| 5.1.3 | Reconstruction of the PSD and the Multilayer Enhancement Factor | 94 |
| 5.2 | Differently Polished Mo/Si/C Multilayers with Molybdenum Thickness Variation | 98 |
| 5.2.1 | Reconstruction of the Interface Morphology | 101 |
| 5.2.2 | Discussion of the Results | 103 |
| 5.3 | Roughness and Intermixing in Cr/Sc Multilayers | 105 |
| 5.3.1 | Estimation of the Vertical Roughness Correlation and the PSD | 107 |
| 5.3.2 | Results and Conclusions | 109 |
| 6 | Summary and Outlook | 111 |
| References | 113 | |

5

Analysis of Interface Roughness based on Diffuse Scattering

(could be)
So far, no distinction was made between interdiffusion or intermixing and roughness at the surface or interfaces. As discussed in detail in Sec. 4.3.4, this distinction based on the employed methods is in fact not possible due to the lack of sensitivity of the experiments conducted there not even for the combination of all methods. Due to the comparatively large beam footprint on the sample in comparison to interfacial roughness on the nanoscale, any specular reflection measurement, and even the measurement of fluorescence radiation generated by a standing wave field, is only sensitive to the average of the interfacial profile and can thus not be distinguished from horizontally homogeneous intermixing. Effectively, both cases can be described with a gradual profile in the optical constants at the interfaces. Consequently, all methods applied so far rely on a horizontally homogeneous medium model, which was reconstructed. The correlation of the roughness parameter σ and the intermixing parameter η in Fig. 4.28 nicely demonstrate that assessment.

*Refl.
(...)
RFZ*

Within this chapter, we investigate the diffuse scattering contribution measured from all samples studied in chapter 4. While none of the experiments conducted there could yield a distinction criterion, diffuse scattering can only be observed from rough surfaces or interfaces, while intermixing does not cause any off-specular intensity contribution. The analysis of the diffuse scattering, here in particular scattering in the EUV spectral range, therefore serves as a natural tool to implement the distinction of intermixing on the one hand and roughness on the other. In addition, the distribution of the scattered intensity contains information on the morphology of roughness which is of particular interest to understand the effect on the reflectivity as observed in the previous chapter. First, we continue the analysis of the Mo/B₄C/Si/C sample based on the layer model derived in Sec. 4.1.1 and demonstrate in detail the effects observed in case of diffuse EUV scattering from multilayer systems with an analysis based on the theory introduced in Sec. 2.4. In the second part, we investigate the two sample sets with systematically varied molybdenum thickness from Sec. 4.2. We specifically focus on the role of the interphase morphology in the diminished reflectivity observed for some of the samples in the two

sets of Mo/Si/C systems. Furthermore, the effect of the polishing process in one of the sample sets is addressed. Finally, we investigate the parameter correlation of intermixing and roughness for the Cr/Sc sample and finalize the characterization made in Sec. 4.3.4 based on the diffuse scattering from that sample.

5.1 Near-normal Incidence Diffuse Scattering

In the theoretical description of diffuse scattering in chapter 2, we have elaborated on the characterization of the scatter intensity from a multilayer sample. The goal of the investigation of the diffuse scattering intensity is to gain information on the interface morphology in the sample. In Sec. 2.2.1, the measured scattering intensity I_s is described in terms of the differential scattering cross section ($\frac{d\sigma}{d\Omega}$), which is given explicitly for the problem of interfacial and surface roughness in multilayer samples in Eq. (2.36). As indicated there, the full theoretical description is based on the introduction of the reciprocal space as an adapted set of coordinates for the scattering problem. This space is spanned by the coordinates q_x , q_y and q_z . Those are the components of the momentum transfer due to the scattering process (cf. Sec. 2.4) and are related to the experimental parameters wavelength λ , as well as the angle of incidence α_i and the exit angle α_f of the scattering experiment. Based on the theory developed in Sec. 2.4, a mapping of reciprocal space along the two coordinates q_x and q_z is required to obtain information on the samples interface morphology.

In order to discuss the diffuse scattering experiments and enable a theoretical analysis, we shall therefore first give some definitions of measurement geometry and how it is related to the reciprocal space coordinates. So far, any scattering measurement (excluding the XRF experiment) of chapter 4 was conducted in the specular reflection geometry, where incidence and exit angle are equal, i.e. at $q_x = q_y \equiv 0$. Diffusely scattered radiation caused by roughness, however, is scattered to off-specular angles. The experiments conducted here are exclusively done in a co-planar geometry since the roughness in the samples under investigation is assumed to be isotropic in the directions parallel to the surface (cf. Sec. 2.4). Thus, any scattered radiation is only measured in the scattering plane defined by the incidence wave vector and the surface normal of the multilayer sample. Two different types of measurements need to be distinguished as they relate to different paths through reciprocal space, the *detector scan* geometry and the *rocking scan* geometry both indicated in Fig. 5.1. The detector scan describes a movement of the detector inside the scattering plane recording radiation scattered to the exit angle α_f , while keeping the incidence angle α_i constant and is indicated by the red shaded area in Fig. 5.1. The rocking scan refers to a rotation of the sample around the axis perpendicular to the scattering plane while keeping the detector position fixed with respect to the incident beam (indicated by the blue shaded area in Fig. 5.1). The angle between detector and the incident beam is referred to as $\Delta\Theta$, while the tilt angle of the sample is ω . By changing ω , the incidence angle α_i and the exit angle α_f are changed accordingly. In both cases this leads to incidence and exit angles, which are no longer equal and, thus, non-vanishing values for the q_x vector component. The out-of-plane angle θ_f (cf. Fig. 2.4 in Ch. 2) remains zero in those experiments and consequently $q_y \equiv 0$.

The corresponding paths through reciprocal space are different for these two cases. They are shown schematically in Fig. 5.2 for two exemplary experimental parameter sets of incidence angle α_i and opening angle $\Delta\Theta$, respectively, as well as wavelength for the

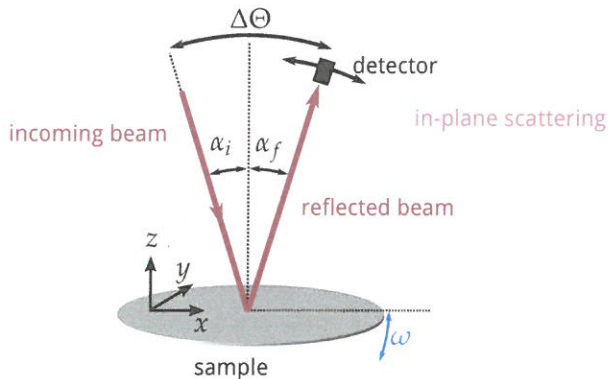


Figure 5.1 | Co-planar measurement geometries. By keeping the opening angle $\Delta\Theta$ between incident and exit beam and the detector fixed, respectively, a rocking scan can be performed by changing the sample angle ω . In a detector scan the sample angle ω is kept fixed and defines the angle of incidence while the detector is moved along Θ .

two scan types. Clearly, for a mapping of the two-dimensional space spanned by q_x

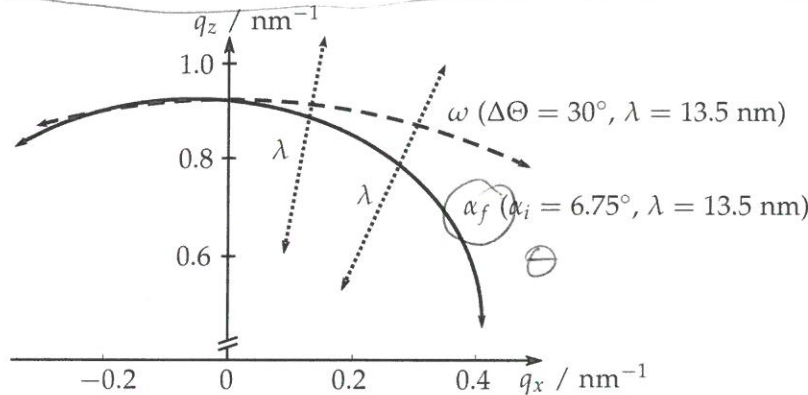


Figure 5.2 | Schematic positions in reciprocal space in dependence on the measurement geometry. The dashed path represents a rocking scan with the angle ω . The solid line shows the movement in q -space when changing the detector angle Θ at a fixed angle of incidence. By tuning the wavelength at each angular position, the q_z -direction becomes accessible as indicated by the dotted arrows.

and q_z it does not suffice to perform only angular scans. In addition, wavelength scans (λ -scan) have to be performed at each angular position. By changing the wavelength and the angle in the same measurement, both degrees of freedom (q_x and q_z) in reciprocal space become accessible.

Based on the theory in Sec. 2.4, interface roughness contributes to the scattering intensity by introducing momentum transfer parallel to the surface. The power spectral density (PSD), describing this statistical roughness, is thus in our co-planar geometry only dependent on q_x^* , i.e. the momentum transfer within the interface planes. In the theory chapter, we have derived an expression for the PSD, which describes an average value across all interfaces of the multilayer. While individual PSDs can be described within the theoretical framework, this poses an ill-defined model for the experiments conducted here. In all measurements taken, many interfaces contribute to the diffuse scattering intensity simultaneously. The periodic character of the multilayer systems, does not allow to distinguish the individual contributions as the wave field inside the

* The PSD is generally dependent on $q_{||} = \sqrt{q_x^2 + q_y^2}$, which reduces to $q_{||} \equiv q_x$ in co-planar geometry

multilayer exhibits the same periodicity. The experiment thus delivers a contribution across all interfaces, which makes a distinction of individual interfaces impossible. In addition to that assessment, the model of a single average PSD is found to be justified in case of high degree of vertical correlation throughout the stack, which we shall confirm through the appearance of the corresponding resonant features in our experiments.

Based on the PSD as derived in Eq. (2.44) with the dependence only on q_x , we should expect to be able to extract its values from the measured data as cuts along the q_x axis anywhere in a measured reciprocal space map. However, it was observed in grazing incidence diffuse x-ray scattering experiments, that vertical correlation of roughness causes an additional intensity modulation of the scattering in reciprocal space along the q_z direction, the so-called *Bragg sheets* [58, 59, 61, 92]. As the interfaces have periodic

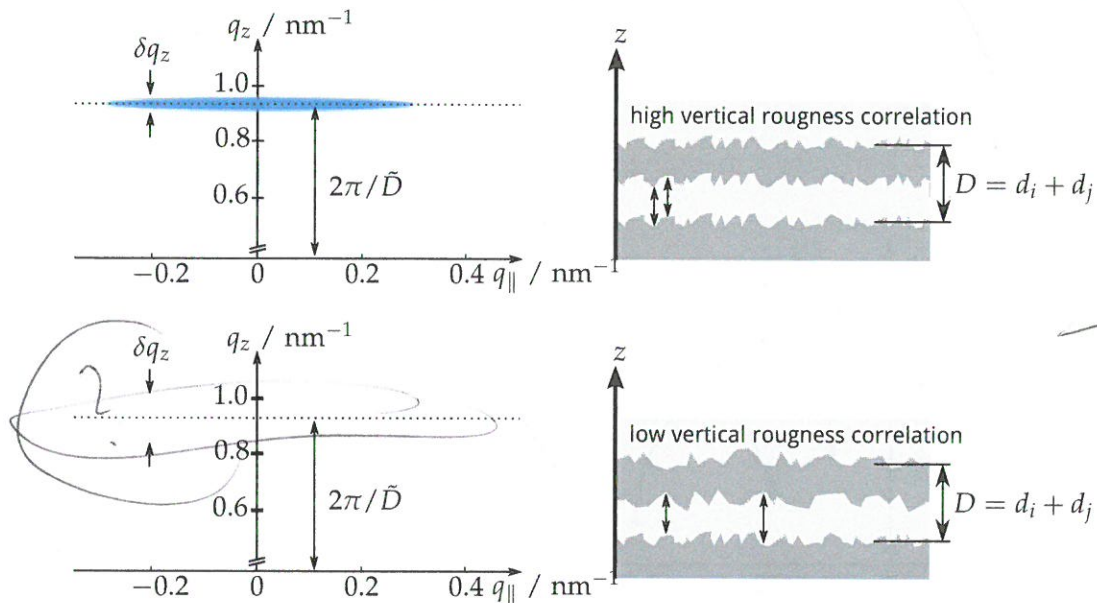


Figure 5.3 | Schematic illustration of the appearance of Bragg-sheets in the off specular scattering intensity at the q_z value fulfilling the Bragg condition of the multilayer stack. The width δq_z of the sheet is dependent on the degree of vertical correlation of roughness.

distances along the surface normal of the sample, roughness correlation poses a Bragg condition with respect to the q_z component of the momentum transfer vector enhancing the diffuse scattering where fulfilled. The expected diffuse scattering distribution in reciprocal space is schematically depicted in Fig. 5.3. Since the periodicity of the interfaces is the multilayer periodicity, those Bragg sheets are expected to appear, where the first and higher order Bragg condition of the multilayer is fulfilled, i.e. where inside the multilayer $q_z = m2\pi/\tilde{D}$. Here, m is the integer number of the Bragg order and $\tilde{D} = \tilde{n}_i d_i + \tilde{n}_j d_j$ is the optical multilayer period thickness in real space, where \tilde{n}_i and \tilde{n}_j are the real part of the index of refraction of the respective layer i and j . Those sheets of increased intensity appearing in reciprocal space vary in width along q_z depending on the strength of the correlation of roughness along the vertical direction in the sample. The higher the correlation, the thinner is the Bragg sheet in q_z -direction (cf. upper and lower part of Fig. 5.3). In the theoretical treatment of the diffuse scattering, this vertical roughness correlation enters as a replication factor in Eq. (2.40) and can be explicitly derived by modeling the layer growth based on the Langevin equation Eq. (2.45) and is given by Eq. (2.48). Due to the strong enhanced intensity in those Bragg sheets, the PSD is

preferably extracted as a vertical cut along q_x at the q_z position of the sheet [92, 101]. Consequently, in the following we shall focus on the mapping of reciprocal space in the vicinity of the first Bragg resonance to observe the expected Bragg-sheet intensity distribution and analyze the interface morphology.

In the studies cited above, the reciprocal space maps of multilayer diffuse scattering were obtained in a grazing incidence geometry using X-rays. The major disadvantage of this technique is that curved samples are not accessible in that way, since no grazing incidence measurement can be conducted if the sample is convexly curved. Here, we study the diffuse scattering using EUV radiation impinging at near-normal incidence. Thereby, this disadvantage is overcome. However, as explained above, using near-normal incidence radiation reduced the accessible q_z range for constant wavelength, which can be compensated by tuning the wavelength accordingly, whereas grazing incidence studies reveal the Bragg sheets in the out-of-plane direction at fixed photon energies, e.g. Siffalovic et al. [101].

5.1.1 Mapping Reciprocal Space for the Mo/B₄C/Si/C Sample

In this section we investigate the EUV diffuse scattering from the Mo/B₄C/Si/C sample discussed in Sec. 4.1 as an example for the analysis of near-normal scatter intensity from multilayer samples. We have conducted diffuse scattering measurements in three different geometries at the SX700 beamline at BESSY II. From the experimental data, the respective reciprocal space coordinates were calculated and the corresponding maps and the experimental details are given in Fig. 5.4.

The reciprocal space maps in Fig. 5.4 for the rocking scan (b) at an opening angle of $\Delta\Theta = 13.5^\circ$ and the rocking scan (c) at an opening angle of $\Delta\Theta = 30^\circ$ and for the detector scan with the angle of incidence $\alpha_i = 6.75^\circ$ clearly show different symmetries rather than the expected Bragg sheet. We observe a strong enhancement in the off-specular scattering around $q_x \approx \pm 0.1 \text{ nm}^{-1}$ (cf. (a) and (c)), which is not replicated on the negative q_x -axis in case of (a). The rocking scans (b) and (c) are symmetric with respect to the specular axis at $q_x = 0$, however, no enhanced scattering appears in (b). The latter map shows a triangular-shaped intensity distribution for both the positive and negative q_x range. A minimum in the width with respect to the q_z direction can be observed here around $q_x \approx \pm 0.2 \text{ nm}^{-1}$. The triangular shape also appears for the positive q_x range of the detector scan in (a), where the minimum in width coincides with the intensity maximum. These observations are in clear contrast to the expectation of an appearance of identical Bragg sheets, independent of the measurement geometry. Clearly, the measurement of diffuse scattering at EUV wavelengths and near-normal incidence differs from the observations made for grazing incidence experiments using X-rays (cf. Salditt et al. [92] or Jiang et al. [61]).

The measurement geometry dependence of the reciprocal space maps indicates that the intensity distributions cannot be the result of multilayer roughness properties alone, i.e. the PSD, which does not change due to changes in the illumination geometry. Scattering intensities caused by roughness occur at identical positions in reciprocal space for any measurement geometry. In fact, the additional modulations of the scatter intensity are caused by the direction from which the radiation impinges on the multilayer structure itself, rather than the roughness properties. We shall therefore consider additional effects that could give an indication for the observations made here.

Fig. 5.3
contrast

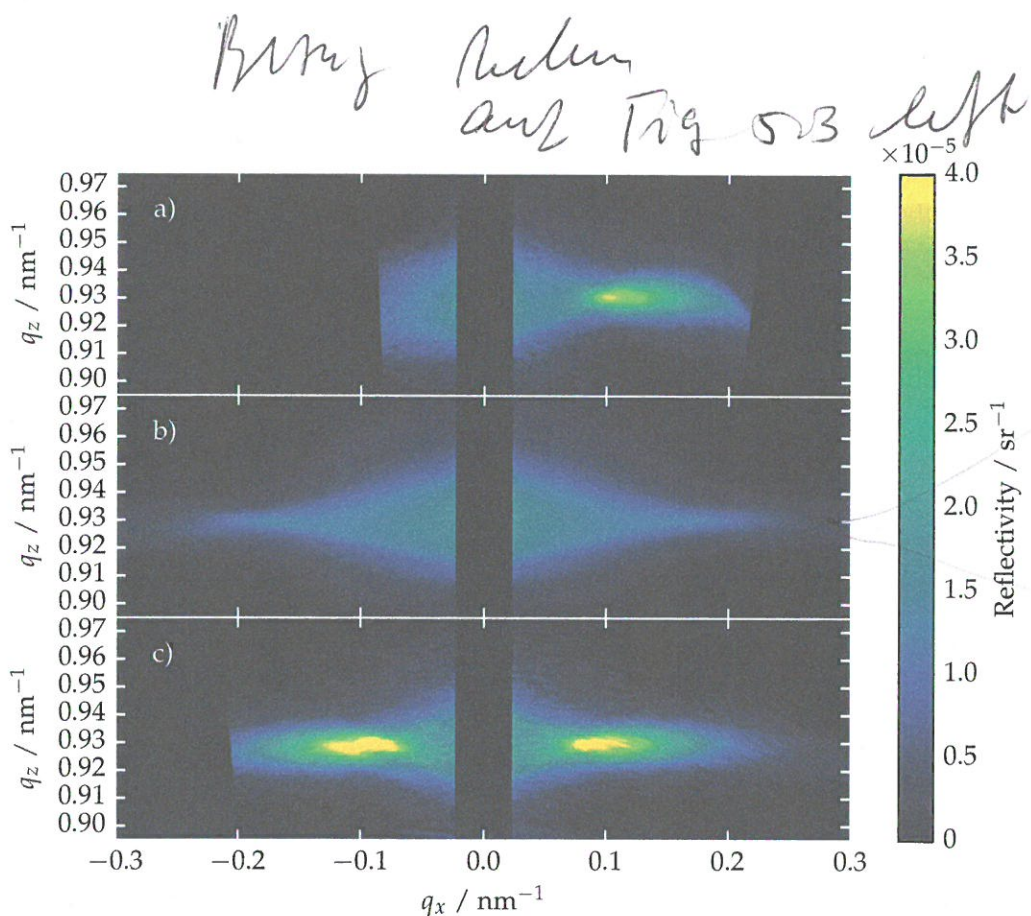


Figure 5.4 | Measured intensity map of a detector scan of the Mo/B₄C/Si/C multilayer mirror at an angle of incidence $\alpha_i = 6.75^\circ$ (a) and measured intensity maps of the identical sample obtained through rocking scans at an opening angle between detector and incident beam of $\Delta\Theta = 13.5^\circ$ (b) and $\Delta\Theta = 30^\circ$ (c). The area close to the specular axis was excluded from this dataset due to its strong intensity compared to the diffuse scattering shown here. The access to the negative q_x -axis in (a) is limited due clipping of the incoming beam with the detector. A GaAsP photo diode with an active area of $4.5 \text{ mm} \times 4.5 \text{ mm}$ at a distance to the sample of 250 mm was used as a detector for the diffusely scattered radiation. The reciprocal space maps were recorded for the two rocking scan geometries (b,c) with an opening angle of $\Delta\Theta = 13.5^\circ$ and of $\Delta\Theta = 30^\circ$ (corresponding to an angle of incidence of $\alpha_i = 6.75^\circ$ and $\alpha_i = 15.0^\circ$, respectively, in specular geometry), respectively, and for the detector scan geometry (a) with the angle of incidence fixed at $\alpha_i = 6.75^\circ$. The first Bragg peak for this multilayer sample, due to its design, is in the wavelength range between 12.4 nm and 14.0 nm . At each angular position of the aforementioned angular scan geometries, a wavelength scan was conducted in this range using a step size of $\Delta\lambda = 0.01 \text{ nm}$. The angular ranges for the rocking scan with opening angle $\Delta\Theta = 13.5^\circ$ correspond to angles of incidence from $\alpha_i = -18.0^\circ$ to $\alpha_i = 31.5^\circ$ in steps of $\Delta\alpha_i = 0.5^\circ$. In terms of the rocking angle ω this range corresponds to values from $\omega = -24.75^\circ$ to $\omega = 24.75^\circ$, where $\omega = 0.0^\circ$ corresponds to the specular reflection geometry ($\alpha_i = \alpha_f$). For the second rocking scan geometry with $\Delta\Theta = 30.0^\circ$, the angle of incidence was varied from $\alpha_i = -3.0^\circ$ to $\alpha_i = 27.5^\circ$ (corresponding to $\omega = -18.0^\circ$ to $\omega = 12.5^\circ$) in steps of 0.5° . Finally, the detector scan was performed at an angle of incidence of $\alpha_i = 6.75^\circ$ moving the detector from $\alpha_f = -3.75^\circ$ to $\alpha_f = 46.75^\circ$ (corresponding to detector angles from $\Delta\Theta = 3.0^\circ$ to $\Delta\Theta = 40.0^\circ$) also in steps of 0.5° .

5.1.2 Kiessig-like Peaks and Resonant Effects

To explain the observed off-specular intensity distribution for the multilayer sample investigated here, additional effects exceeding the description of Bragg sheets need to be taken into account. So far, the description of diffuse scattering and enhancement due to correlated roughness was under the assumption of kinematic scattering, i.e. a single diffuse scattering event. However, multiple reflections at the interfaces may not be ignored. To clarify that, we shall consider two additional processes, which may happen before and after a diffuse scattering event at the interface. Fig. 5.5 illustrates two situations, where the impinging or exiting (diffusely scattered) radiation is in resonance with the multilayers Bragg condition, i.e. strongly enhanced in intensity. In the first case

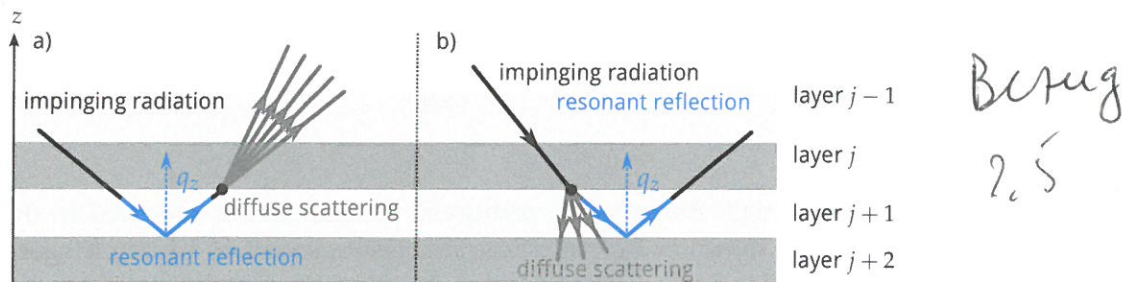


Figure 5.5 | Illustration of dynamic scattering processes. In (a), the impinging radiation is resonantly reflected from the multilayer structure by fulfilling the Bragg condition. In (b), certain parts of the diffusely scattered radiation from the interface roughness again fulfills the Bragg condition and is enhanced in intensity.

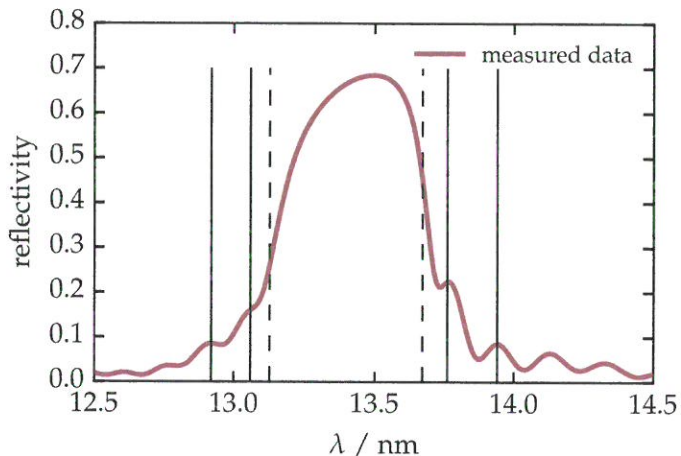
(a), the impinging radiation fulfills the Bragg condition with respect to angle of incidence and is consequently resonantly reflected from the multilayer mirror. Through this, any diffusely scattered radiation measured at any exit angle would be significantly stronger compared to the situation, where the incidence angle or wavelength does not fulfill the Bragg condition, despite the fact that the roughness itself did not change. In the second case (b), depending on the wavelength some of the diffusely scattered radiation fulfills the Bragg condition of the multilayer and is again reflected resonantly from it causing a major intensity increase.

Those effects are the result of multiple (dynamic) reflections inside the multilayer system. They were observed as resonantly enhanced streaks, so-called *Bragg-like lines*, and intense *Bragg-like peaks*, where both the conditions illustrated in Fig. 5.5 are fulfilled. Often observed in diffuse scattering maps from multilayer samples recorded in grazing incidence geometry with X-rays [58]. The theoretical principle leading to these off-specular enhancements is also known as the process of *Umweganregung* [11, 12]. As the fulfillment of the Bragg condition is only dependent on two of the three experimental parameters, i.e. either the incidence angle α_i or the exit angle α_f in both cases together with the wavelength, the position of those enhancements is different in the reciprocal space map depending on the measurement geometry. In literature [11, 12, 58, 78], such enhancements were so far only observed from the main Bragg resonance of the multilayer, i.e. the fulfillment of the Bragg condition of the periodic stack. In our case no higher order Bragg resonances can be observed, as they would appear as Bragg-like peaks in the off-specular scattering far away from the accessible q_{\parallel} range of our experiment. However, the two Bragg-like lines corresponding to the first order Bragg peak cross at the position

entweder
oder ?

of the specular reflex and otherwise amount to broad bands in the diffuse map as we shall elaborate in the following.

Figure 5.6 | Measured reflectivity curve of the Mo/B₄C/SiC multilayer mirror at an angle of incidence $\alpha_i = 6.75^\circ$. The solid black lines mark the positions of the first two Kiessig-fringes at each side of the main maximum. The dashed lines indicate the full width at half maximum (FWHM) position of the main Bragg peak.



Apart from the main Bragg peak, additional resonances are observed in the EUV reflectivity curve as shown in Fig. 5.6. Those side peaks, known as Kiessig fringes [63] as previously discussed in Sec. 4.1, correspond to the interference of radiation reflected from the top surface and the substrate interface. The dynamic enhancement expected for those side fringes is very well within the measured reciprocal space ranges of our measurements geometries and wavelengths. In Fig. 5.7 the positions where those enhancements are expected in the maps shown in 5.4 are indicated as white solid lines for the first two fringes on either side of the reflectivity curve maximum. In addition, the FWHM of the main Bragg maximum was marked with dashed lines. Clearly, the off-specular enhancement observed fits to the theoretically predicted appearance of Bragg-like peaks, i.e. at the crossing points of the lines, which we shall call *Kiessig-like peaks*, due to their origin. The strong enhancement, however, is only observed where there is also a Bragg sheet due to correlated roughness. The aforementioned broad bands corresponding to the Bragg-like lines of the main Bragg resonance appear in between the dashed lines. Indeed, most prominently visible in Fig. 5.7b, the triangular shaped intensity distribution in the center of the map is in fact the result of resonant enhancement due to the first order Bragg-like peak, which extends across a large area of the map in this case. The diffuse scattering distribution in the reciprocal space maps is thus a combination of dynamic effects (the first-order Bragg-like peak and the Kiessig-like peaks) and kinematic effects (Bragg sheets).

The processes described here are contained in the theoretical description given in Eq. (2.51) in Sec. 2.4. They correspond to the contributions of the distorted-wave Born approximation (DWBA) differential cross section through the processes shown in Fig. 2.5, labeled *RT** and *TR** (Kiessig-like lines, Bragg-like lines) and *RR** (Kiessig-like peaks, Bragg-like peaks). The Bragg-sheets, however, are described as a simple fulfillment of the Bragg condition due to the momentum transfer at the interfaces according to the semi-kinematic description labeled *TT**. In order to assess the contribution of dynamic multiple reflections within the stack, we compared the semi-kinematic approximation in Eq. (2.37) with the dynamic calculations in Eq. (2.51). In the semi-kinematic case, all multiple reflection effects are ignored in the differential cross section. The result is the intensity distribution as expected from the kinematic case, however including the accurate transmitted field amplitudes at each interface instead of only a plane wave field

5.5

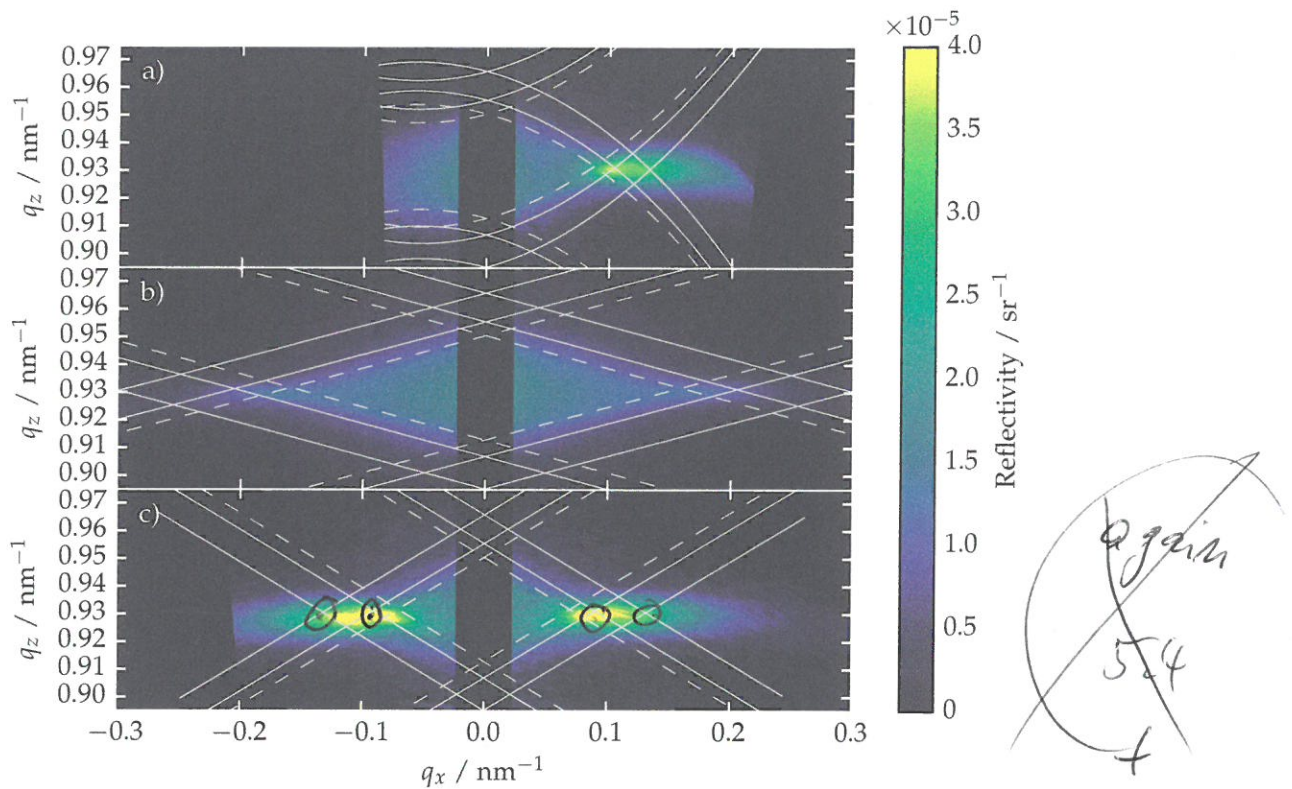


Figure 5.7 | Measured intensity maps of Fig. 5.4 with the calculated positions of the Kiessig-like lines (solid lines) for the Kiessig fringes marked in Fig. 5.6 and the Bragg-like lines (bands between the dashed lines). The positions, where the solid lines cross show the Kiessig-like peaks positions. The area contained within the dashed lines in the center of each plot correspond to the Bragg-like peak of the first Bragg order of the multilayer and explain the triangular or diamond shaped area of increased intensity (see main text).

*6
Kiessig
Peak : Schmidspeck*

amplitude as in the simple Born approximation. For this comparison, we simulated the rocking scan at an opening angle of $\Delta\Theta = 30^\circ$. The roughness properties for these simulations were determined following the procedure described below in Sec. 5.1.3 to match the samples properties*.

To evaluate the contribution of multiple reflections due to the subsidiary maxima, Fig. 5.8b shows the intensity distribution along q_x at $q_z = 0.93 \text{ nm}^{-1}$ again in comparison to the EUV reflectivity curve in Fig. 5.8a. The solid blue line corresponds to the dynamic

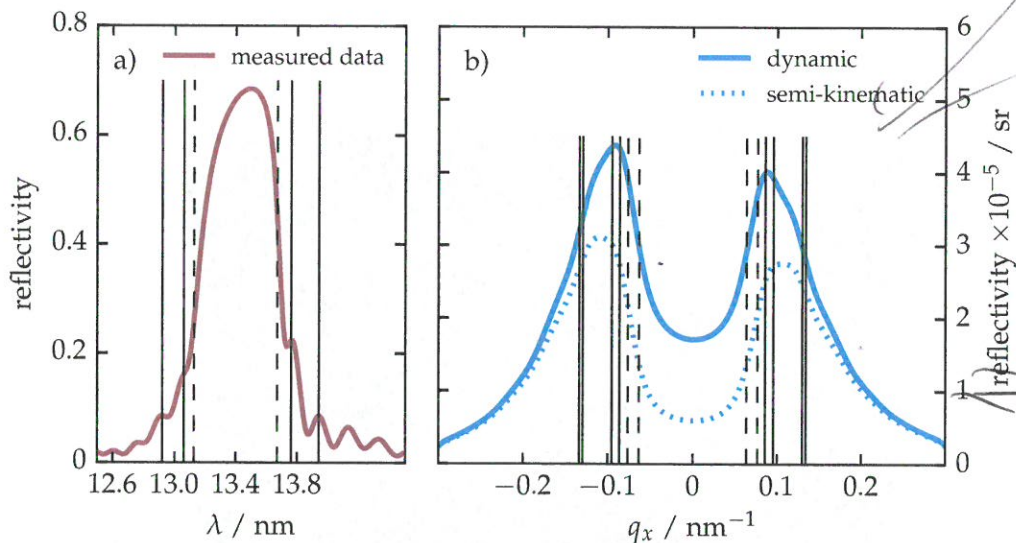


Figure 5.8 | a) EUV reflectivity curve with the positions of the FWHM of the Bragg peak (dashed black lines) and the positions of the first two Kiessig fringes on each side of the main maximum (solid black lines) similar to Fig. 5.6. b) Calculated scattering intensity distribution at $q_z = 0.93 \text{ nm}^{-1}$. The solid blue line shows the result of the dynamic calculation for a rocking scan with an opening angle of $\Delta\Theta = 30^\circ$. The dashed blue line represents the calculation applying the semi-kinematic approximation, ignoring any multiple reflections within the multilayer. The dashed vertical lines are the position of the main Bragg peaks FWHM, while the solid vertical lines show the position of dynamic contributions of the Kiessig fringes close to the main maximum. Each Kiessig fringe marked in the inset appears for the corresponding positive and negative q_x value. The strong intensity at $|q_x| \approx 0.1 \text{ nm}^{-1}$ results from the overlap of the dynamic maxima of two different Kiessig fringes (see text).

theory, while the dotted blue line is the result of the semi-kinematic calculation. The dashed vertical lines indicate the limits of the main Bragg peaks FWHM. The vertical black lines show the position of the Kiessig-like lines intersecting the cut position. Each of the marked fringes in Fig. 5.8a appears on the negative and positive q_x -axis in Fig. 5.8b. This is caused by the incidence and exit angle, respectively, being at the resonance angle of the various Kiessig maxima in the reflectivity curve as illustrated in Fig. 5.5. A strong increase with respect to the semi-kinematic approximation is observed. The position of the dynamic contribution from the first Kiessig fringes on either side of the main resonance exhibits a pronounced maximum in the diffuse scattering. These fringes contribute most due to their high overall relative intensity compared with the fringes further away from the reflectivity maximum. In addition, the position in reciprocal space coincides with the first two Kiessig fringes marked on either side of the main maximum. The contribution by the main Bragg resonance, i.e. the Bragg-like peak

* In Sec. 4.1.1, a reconstruction based on the measurement of EUV reflectivity curves was found and the values listed in table 4.3 serve as the model parameters for the analysis conducted here.

amounts to approximately 100% at $q_x = 0$. The comparison to the semi-kinematic case reveals another reason for the strong intensity of the Kiessig-like peaks compared to the Bragg-like peak. In between the dashed lines on the positive and negative q_x axis in Fig. 5.8b, a significant decrease of kinematically scattered radiation is observed. The reason for that is a strongly diminished penetration depth of the radiation into the multilayer at the Bragg resonance, which causes less rough interfaces to contribute to the diffuse scattering. This directly counteracts the resonant enhancement due to the Bragg-like peak and leads to an overall lower scattering contribution at these positions in reciprocal space.

A quantitative comparison of the dynamic contribution to the total scattering intensity in our measurements is shown in Fig. 5.9 as a line cut along the q_z at $q_x = 0.05 \text{ nm}^{-1}$, perpendicular to the simulations shown in Fig. 5.8. The dynamic calculation yields

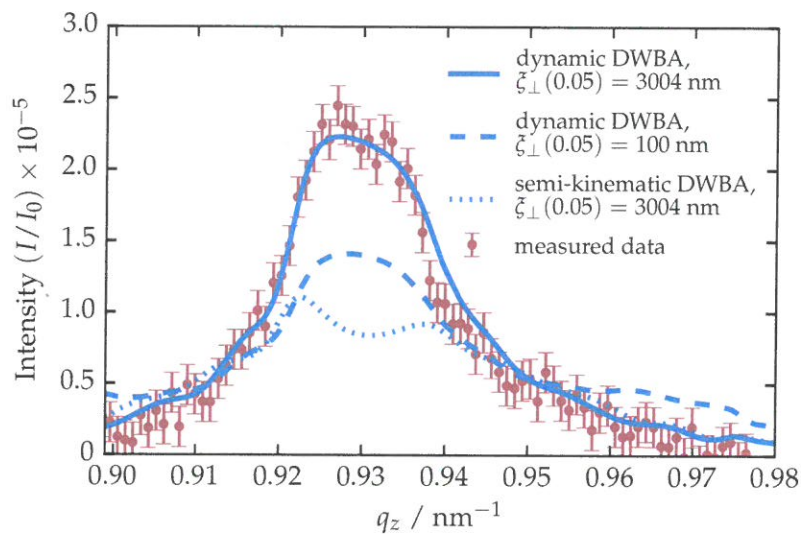


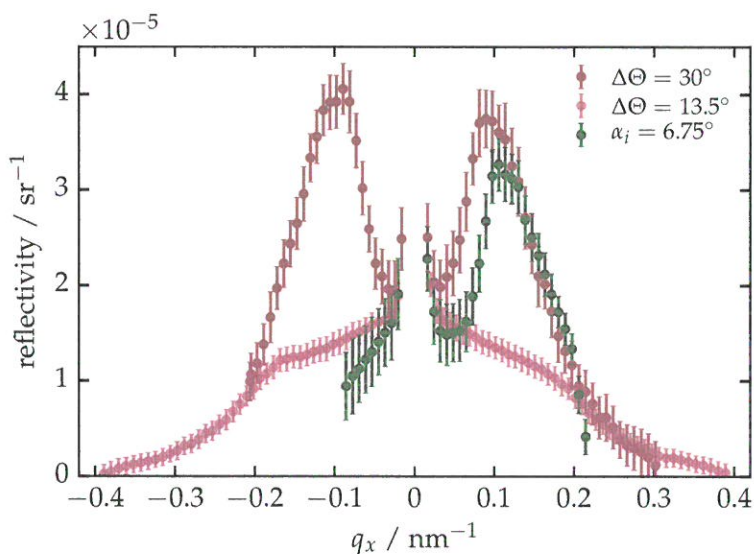
Figure 5.9 | Scattering intensity along q_z for $q_x = 0.05 \text{ nm}^{-1}$ for the dynamic and semi-kinematic calculations for a rocking scan at $\Delta\Theta = 30^\circ$ in comparison to the measured data.

excellent agreement with the measured data with the PSD and correlation parameters obtained following the procedure explained in Sec. 5.1.3. The results show distinct differences with an increase up to 100% of the scattered intensity close to the multilayer resonance at $q_z = 0.93 \text{ nm}^{-1}$ compared to the semi-kinematic calculation. Hence the dominance of the dynamic contributions in the vicinity of the Bragg resonance is also observed here. In addition to comparing the dynamic and semi-kinematic calculations, a dynamic calculation assuming a reduced vertical correlation of roughness was added as dashed blue curve. As discussed in the beginning of Sec. 5.1, the Bragg sheet width is strongly dependent on the amount of correlated interfaces. Clearly, a broadening and reduction of scatter intensity is seen for this case here. This shows, that the Bragg sheet is in fact still visible but obscured by the dominant structure in the diffuse scattering caused by the dynamic effects explained above.

5.1.3 Reconstruction of the PSD and the Multilayer Enhancement Factor

The large impact of resonant effects on the off-specular scattering intensity measured in the three geometries shown above prove, that multiple reflections have to be taken into account to extract the contribution of the interface morphology and determine a PSD. To better understand the effects involved here, we shall analyze the intensity curves for all three measurement geometries based on a horizontal cut along q_x at the position of $q_z = 0.93 \text{ nm}^{-1}$, which corresponds to the momentum transfer at the multilayer resonance and thus the maximum of the Bragg sheet and contain the PSD analogous to Siffalovic et al. [101]. The intensity curves are shown in direct comparison in Fig. 5.10. The strong

Figure 5.10 | Averaged diffuse scattering intensity along q_x in the interval $q_z = (0.930 \pm 0.003) \text{ nm}^{-1}$ corresponding to the resonance of the multilayer. The data shown are two rocking scan and one detector scan geometries (see text for details).



off-specular enhancement of scattering intensity is clearly visible here for the detector scan geometry and the rocking scan with opening angle of $\Delta\Theta = 30.0^\circ$. In case of the second rocking scan with $\Delta\Theta = 13.5^\circ$, only a small shoulder can be observed at $q_x \approx \pm 0.2 \text{ nm}^{-1}$.

In the theoretical treatment of the diffuse scattering, we have derived an expression for the differential cross section based on the DWBA. It separates the dynamic enhancements and penetration depth considerations from the power spectral density contribution. The corresponding equation (cf. Eq. (2.51)), is given by

$$\left(\frac{d\sigma}{d\Omega} \right)_{\text{DWBA}} = \left[\frac{A\pi^2}{\lambda^4} \sum_{j=1}^N \sum_{i=1}^N (n_j^2 - n_{j+1}^2)^* (n_i^2 - n_{i+1}^2)^* ((T_j^{(1)} + R_j^{(1)})^* (T_j^{(2)} + R_j^{(2)})^* \times (T_i^{(1)} + R_i^{(1)}) (T_i^{(2)} + R_i^{(2)})) \exp(-iq_x \tan \beta (z_i - z_j)) c_{\perp}^{ij} \right] C(q_x). \quad (5.1)$$

The equation is colored to indicate the two parts of interest. The blue colored factor contained in rectangular brackets is the dynamic and kinematic part due to the scattering properties from a multilayer and only dependent on the multilayer layout, we therefore refer to it as *multilayer enhancement factor*. The red colored term $C(q_x)$, is the average power spectral density and describes the average interface morphology.

To illustrate the impact due to the presence of the multilayer and the geometry dependence, the result of calculations of the multilayer enhancement factor alone, based on the layer model of our multilayer sample is shown in Fig. 5.11 for the detector scan and the two rocking scan configurations. The multilayer enhancement factor was normalized with respect to $q_x = 0$, i.e. the calculated diffuse scattering contribution on the specular axis. It should be noted here, that the abrupt drop observed for each of the curves

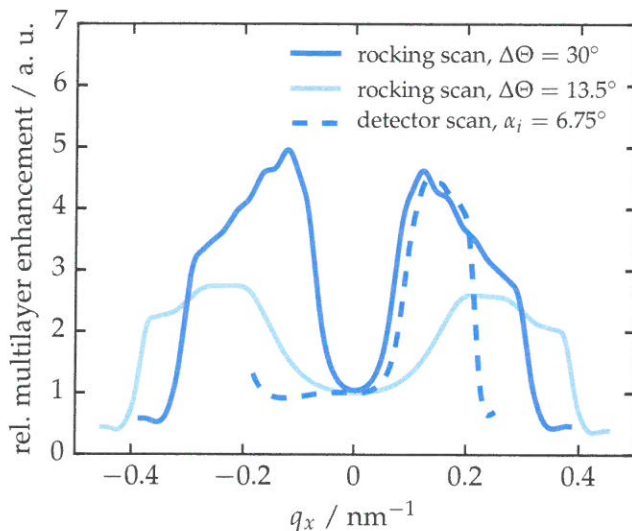


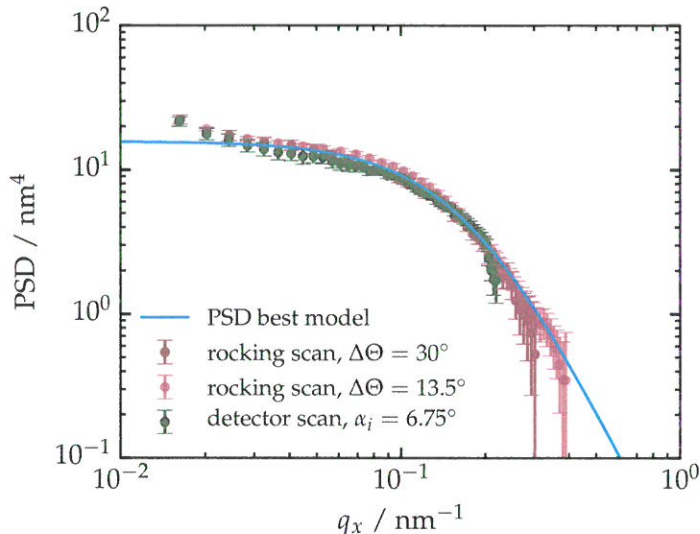
Figure 5.11 | Enhancement factor due to the specific properties of multilayer reflectivity for three different measurement geometries. The simulations shown here were normalized with respect to the diffuse contribution to the specular reflectivity at $q_x = 0$.

towards higher q_x values is not the result of a breakdown of vertical correlation. Instead, it marks the point in reciprocal space for each geometry, respectively, where the photon energy is in resonance with the Si-L edge causing a strong increase of absorption and thus a sharp decrease of the penetration depth into the multilayer. As a result, diffuse scattering intensity is decreased significantly.

The results of the calculation above show that the diffuse scattering from these multilayer mirror systems at near-normal incidence exhibits strong enhancement due to the intrinsically limited bandpass of reflectivity and high reflectance. If both the incidence and exit angle is out of the Bragg resonance, the higher penetration depth of the multilayer causes an increase in the number of interfaces contributing to the diffuse scattering intensity. Thus higher total scattering is observed. The Kiessig fringes and the main Bragg peak cause modulations in the enhancement factor increased by the purely dynamic processes described in the previous section. Based on the results, the cuts along q_x shown in Fig. 5.10 through the three measured maps from this sample could be normalized to extract the PSD of the sample. The result is shown in Fig. 5.12 for the positive q_x range. Clearly, this result shows a consistent determination for the PSD, with the individual cuts being in agreement within the measurement uncertainty. Based on the calculation of the multilayer enhancement factor, experimental curves for the PSD can be extracted as shown in Fig. 5.12 without applying a specific model for the interface morphology. However, the measurements conducted here only deliver data in a limited range in the reciprocal space, depending on the selected geometry and wavelengths. To characterize the interface morphology, it is therefore necessary to model the measured data and deduct parameters that relate to the roughness properties. To obtain the PSD best model reconstruction, the PSO method was employed similarly to the reconstructions shown in the previous chapter. The details of this analysis will be

are shown
?

Figure 5.12 | Diffuse scattering intensity corrected for the multilayer enhancement factor. The blue solid line corresponds to a power spectral density with $\xi_{\parallel} = 5.6 \text{ nm}$, $H = 1.0$, $\sigma = 0.2 \text{ nm}$ and a vertical correlation length of $\xi_{\perp}(q_x) = 7.5/q_x^2 \text{ nm}^{-1}$.



given in the following paragraph.

Reconstruction of the Power Spectral Density

Within the framework of the DWBA, considering the dynamic effects the full expression for the differential cross section of the diffuse scatter is given in Eq. (5.1). As discussed above, the power spectral density only becomes accessible through the diffuse scattering measurements, if the structural properties of the multilayer are known. Those were determined for all samples in this thesis with the methods described in chapter 4. Based on those results, the differential cross section allows to calculate the scattering intensity maps, which were measured here and therefore enable the reconstruction of the PSD.

It is the goal of this analysis to deduct key properties of the interface roughness, such as vertical and lateral correlation lengths and the r.m.s. roughness value σ_r . The latter is directly related to the Néerot-Croce parameter σ , while there intermixing at the interfaces is also contained as it can not be distinguished from the roughness. Based on the analysis of the PSD, this distinction can be made. To reconstruct the PSD, a suitable model has to be introduced for the interface morphology. Here, we apply a fractal interface model, which was found to adequately describe the roughness in case of sputter deposited multilayer systems [19, 20, 103]. It should be noted, that the PSD for a two dimensional surface should be two-dimensional itself and consider possibly different roughness properties in x (q_x) and y (q_y) direction. The samples we are investigating here, however, are fabricated using magnetron sputtering and on rotating sample holders as shown in Sec. 3.4.2. This is important to achieve a homogeneous deposition. We therefore conclude, that roughness on the surfaces and interfaces does not have any predominant direction and may be assumed to be isotropic, i.e. only dependent on the absolute value of the lateral momentum transfer vector $q_{\parallel} = \sqrt{q_x^2 + q_y^2}$. The PSD can then be expressed in the closed analytical one-dimensional form as shown in Eq. (2.44). The three parameters describing the fractal nature of the roughness are the lateral correlation length ξ_{\parallel} , the r.m.s. roughness σ_r and the Hurst factor H . The vertical correlation of the roughness parameter ξ_{\perp} and the off-axis roughness correlation angle β , however, are not included in the PSD as they are part of the multilayer enhancement factor. In order to fully characterize the system, we therefore analyze the full data set comprising all

Table 5.1 | Parameters of the DWBA analysis. The lower bound (LB) and upper bound (UB) specify the PSO parameter space limits.

| Parameter | Definition | LB | UB | PSO result |
|----------------------------------|---|-------|------|------------|
| σ_r / nm | root mean square roughness | 0.0 | 1.0 | 0.201 |
| ξ_{\parallel} / nm | lateral correlation length | 0.0 | 20.0 | 5.579 |
| ξ_{\perp} / nm ⁻¹ | vertical correlation parameter yielding vertical correlation length trough $\tilde{\xi}_{\perp}(q_{\parallel}) = \xi_{\perp}/q_{\parallel}^2$ | 0.0 | 20.0 | 7.512 |
| H | Hurst factor | 0.0 | 1.0 | 1.000 |
| β / ° | angle for off-axis vertical roughness correlation | -10.0 | 10.0 | -0.152 |

data points measured for the reciprocal space maps. As explained above, the maps were measured by performing wavelength scans at each angular position of the rocking or detector scans. The result are intensity curves $I_{(\alpha_i, \alpha_f)}(\lambda)$, for each set of angular positions in dependence on the wavelength. The minimization functional $\tilde{\chi}^2$ for each of the three experiments (three diffuse scattering maps), is thus given by

$$\tilde{\chi}^2 = \frac{1}{M - P} \sum_{(\alpha_i, \alpha_f)} \sum_m \frac{(I_m^{\text{model}}(\alpha_i, \alpha_f, \lambda) - I_m^{\text{meas}}(\alpha_i, \alpha_f, \lambda))^2}{\tilde{\sigma}_m^2}, \quad (5.2)$$

where M is the total number of measurement points, P is the number of optimization parameters and (α_i, α_f) indicates a specific position in the angular detector or rocking scans. The reconstruction was achieved by applying the PSO technique on the combined set of measurements from all three experiments, i.e. minimizing the functional $\chi^2 = \tilde{\chi}_a^2 + \tilde{\chi}_b^2 + \tilde{\chi}_c^2$. The letter indices a, b and c refer to the reciprocal space maps shown in Fig. 5.4. The optimization model parameters are listed in table 5.1 together with the converged results found. In Fig. 5.13, the measured reciprocal space maps in the detector scan geometry and the rocking scan geometry are shown in direct comparison with the theoretically calculated maps based on the best model results. The calculated reciprocal space maps are in good agreement with the measured data. The results reveal a strong correlation of the roughness throughout the multilayer stack. Indeed, the correlation length extends across the whole multilayer stack up to spacial frequencies of $q_{\parallel} \approx 0.13 \text{ nm}^{-1}$. Beyond that frequency the correlation length reduces to values lower than the total stack thickness according to the relation $\tilde{\xi}_{\perp}(q_{\parallel}) = \xi_{\perp}/q_{\parallel}^2$. The average PSD parameters obtained show a r.m.s. roughness of $\sigma_r = 0.201 \text{ nm}$, which is in agreement with the value $\sigma = 0.214 \text{ nm}$ ($-0.143 \text{ nm} / + 0.201 \text{ nm}$) obtained in the MCMC analysis conducted in Sec. 4.1.1 for the Nérot-Croce parameter. It thus may be concluded that roughness is the dominant disturbance relevant for diminished reflectivity for that sample and the interdiffusion barriers provide effective means to hinder intermixing.

In conclusion, the analysis of diffuse scatter presented here provides a powerful method for the reconstruction of the average PSD of the interfaces inside the multilayer. In comparison to techniques such as atomic force microscopy (AFM), which solely measure at the top surface, it can deliver data on the interface properties inside the multilayer. In addition it provides information on a large area of the surface and the interfaces. The near-normal incidence angles used in the measurement allow to study potentially strongly curved multilayer mirrors, which are often implemented in optical

Unc. ?

+ data
of chapt

for
Fig 5.4

$\tilde{\xi}_{\parallel} = 5.6 \text{ nm}$

unc.?

Uncertainty
discuss

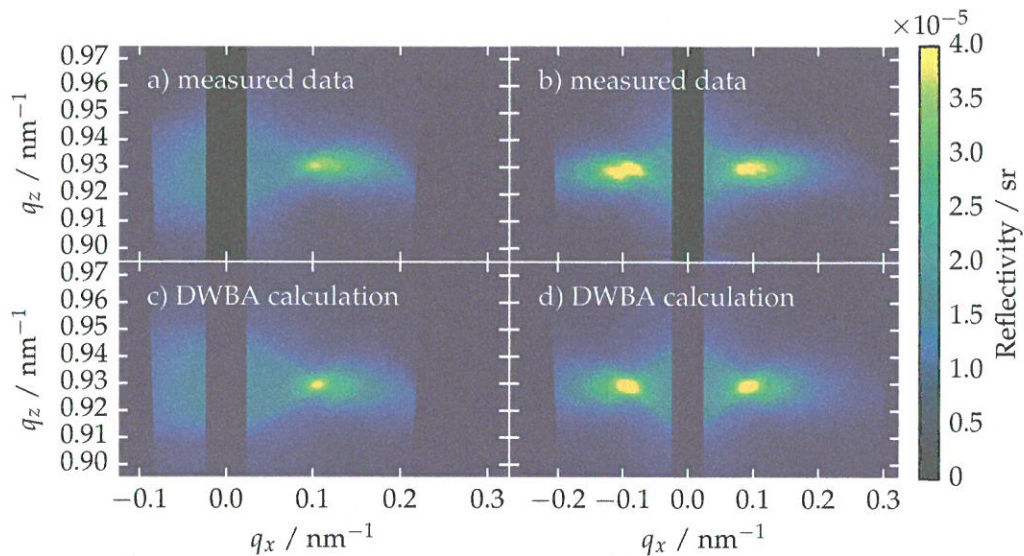


Figure 5.13 | Measured reciprocal space maps for the detector scan geometry (a) and the rocking scan at an opening angle of $\Delta\Theta = 30^\circ$ (b). The corresponding calculated maps based on the PSO results are shown in direct comparison in (c) and (d) for the respective scan geometries.

setups, and thus provides an advantage to established grazing-incidence methods of measuring diffuse scattering. Due to the experimental access to the interface morphology based on this technique, the assessment of which interface disturbances cause a loss of reflectivity compared to simulations based on perfect chemically abrupt interfaces provides interesting insights on the sample properties and extends the capabilities of characterization established in chapter 4. With that, the improvement of the fabrication of such optics may become possible, knowing which effects need to be counteracted to reach higher reflectivities. Parts of the results of the analysis in Sec. 4.1 and the findings of this section were published in A. Haase, V. Soltwisch, C. Laubis and F. Scholze: ‘Role of dynamic effects in the characterization of multilayers by means of power spectral density’. In: *Appl. Opt.* **53**.14 (2014), pp. 3019–3027. doi: 10.1364/AO.53.003019.

5.2 Differently Polished Mo/Si/C Multilayers with Molybdenum Thickness Variation

In Sec. 4.2, we have reconstructed the multilayer model of two sample sets of polished and unpolished Mo/Si/C multilayer mirrors with a varying relative thickness of the molybdenum layer from sample to sample. The findings there show the appearance of significant drops in the peak reflectivity at certain thickness values correlated with jumps in the total period thickness, different depending on to which set, polished or unpolished, the samples belong to. Here, we shall apply the method to analyze the diffuse scattering detailed above to the two sample sets investigated in the previous chapter. The goal of this is to assess the effect of the presumed crystallization at a certain molybdenum thickness threshold on the interface morphology and, thus, investigate the origins of the reflectivity drops that are shown in Fig. 4.14.

For that purpose, only for selected samples in the vicinity of the presumed crystallization threshold in both sets, as well as far away from that molybdenum thickness

Table 5.1 | Parameters of the DWBA analysis. The lower bound (LB) and upper bound (UB) specify the PSO parameter space limits.

| Parameter | Definition | LB | UB | PSO result |
|----------------------------------|---|-------|------|------------|
| σ_r / nm | root mean square roughness | 0.0 | 1.0 | 0.201 |
| ξ_{\parallel} / nm | lateral correlation length | 0.0 | 20.0 | 5.579 |
| ξ_{\perp} / nm ⁻¹ | vertical correlation parameter yielding vertical correlation length trough $\tilde{\xi}_{\perp}(q_{\parallel}) = \xi_{\perp}/q_{\parallel}^2$ | 0.0 | 20.0 | 7.512 |
| H | Hurst factor | 0.0 | 1.0 | 1.000 |
| β / ° | angle for off-axis vertical roughness correlation | -10.0 | 10.0 | -0.152 |

data points measured for the reciprocal space maps. As explained above, the maps were measured by performing wavelength scans at each angular position of the rocking or detector scans. The result are intensity curves $I_{(\alpha_i, \alpha_f)}(\lambda)$, for each set of angular positions in dependence on the wavelength. The minimization functional $\tilde{\chi}^2$ for each of the three experiments (three diffuse scattering maps), is thus given by

$$\tilde{\chi}^2 = \frac{1}{M - P} \sum_{(\alpha_i, \alpha_f)} \sum_m \frac{(I_m^{\text{model}}(\alpha_i, \alpha_f, \lambda) - I_m^{\text{meas}}(\alpha_i, \alpha_f, \lambda))^2}{\tilde{\sigma}_m^2}, \quad (5.2)$$

where M is the total number of measurement points, P is the number of optimization parameters and (α_i, α_f) indicates a specific position in the angular detector or rocking scans. The reconstruction was achieved by applying the PSO technique on the combined set of measurements from all three experiments, i.e. minimizing the functional $\chi^2 = \tilde{\chi}_a^2 + \tilde{\chi}_b^2 + \tilde{\chi}_c^2$. The letter indices a, b and c refer to the reciprocal space maps shown in Fig. 5.4. The optimization model parameters are listed in table 5.1 together with the converged results found. In Fig. 5.13, the measured reciprocal space maps in the detector scan geometry and the rocking scan geometry are shown in direct comparison with the theoretically calculated maps based on the best model results. The calculated reciprocal space maps are in good agreement with the measured data. The results reveal a strong correlation of the roughness throughout the multilayer stack. Indeed, the correlation length extends across the whole multilayer stack up to spacial frequencies of $q_{\parallel} \approx 0.13 \text{ nm}^{-1}$. Beyond that frequency the correlation length reduces to values lower than the total stack thickness according to the relation $\tilde{\xi}_{\perp}(q_{\parallel}) = \xi_{\perp}/q_{\parallel}^2$. The average PSD parameters obtained show a r.m.s. roughness of $\sigma_r = 0.201 \text{ nm}$, which is in agreement with the value $\sigma = 0.214 \text{ nm} (-0.143 \text{ nm} / +0.201 \text{ nm})$ obtained in the MCMC analysis conducted in Sec. 4.1.1 for the Nérot-Croce parameter. It thus may be concluded that roughness is the dominant disturbance relevant for diminished reflectivity for that sample and the interdiffusion barriers provide effective means to hinder intermixing.

In conclusion, the analysis of diffuse scatter presented here provides a powerful method for the reconstruction of the average PSD of the interfaces inside the multilayer. In comparison to techniques such as atomic force microscopy (AFM), which solely measure at the top surface, it can deliver data on the interface properties inside the multilayer. In addition it provides information on a large area of the surface and the interfaces. The near-normal incidence angles used in the measurement allow to study potentially strongly curved multilayer mirrors, which are often implemented in optical

+ data
of depth
from
Fig 5.1

$\tilde{\xi}_{\parallel} = 5.6$
unc. ?

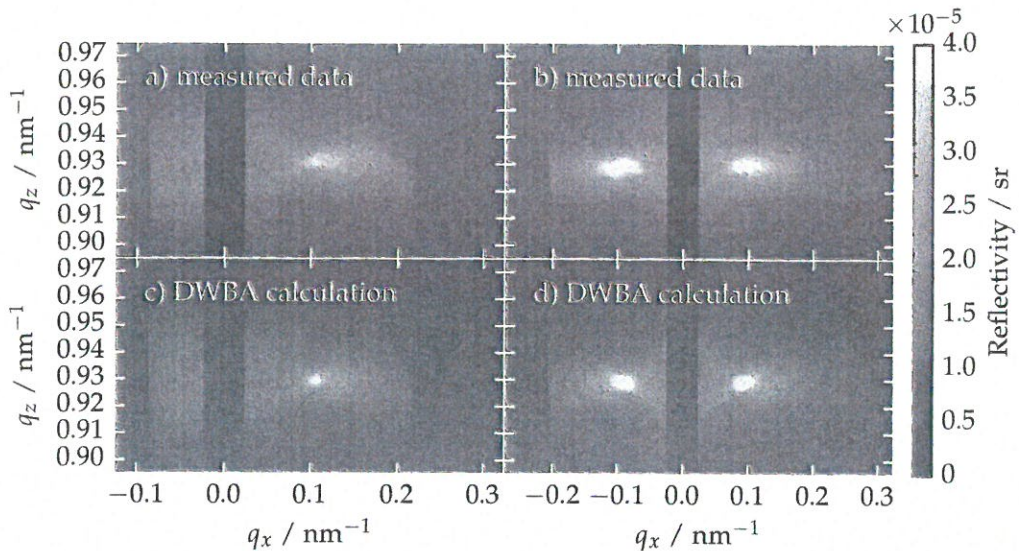


Figure 5.13 | Measured reciprocal space maps for the detector scan geometry (a) and the rocking scan at an opening angle of $\Delta\Theta = 30^\circ$ (b). The corresponding calculated maps based on the PSO results are shown in direct comparison in (c) and (d) for the respective scan geometries.

setups, and thus provides an advantage to established grazing-incidence methods of measuring diffuse scattering. Due to the experimental access to the interface morphology based on this technique, the assessment of which interface disturbances cause a loss of reflectivity compared to simulations based on perfect chemically abrupt interfaces provides interesting insights on the sample properties and extends the capabilities of characterization established in chapter 4. With that, the improvement of the fabrication of such optics may become possible, knowing which effects need to be counteracted to reach higher reflectivities. Parts of the results of the analysis in Sec. 4.1 and the findings of this section were published in A. Haase, V. Soltwisch, C. Laubis and F. Scholze: 'Role of dynamic effects in the characterization of multilayers by means of power spectral density'. In: *Appl. Opt.* 53.14 (2014), pp. 3019–3027. doi: 10.1364/AO.53.003019.

5.2 Differently Polished Mo/Si/C Multilayers with Molybdenum Thickness Variation

In Sec. 4.2, we have reconstructed the multilayer model of two sample sets of polished and unpolished Mo/Si/C multilayer mirrors with a varying relative thickness of the molybdenum layer from sample to sample. The findings there show the appearance of significant drops in the peak reflectivity at certain thickness values correlated with jumps in the total period thickness, different depending on to which set, polished or unpolished, the samples belong to. Here, we shall apply the method to analyze the diffuse scattering detailed above to the two sample sets investigated in the previous chapter. The goal of this is to assess the effect of the presumed crystallization at a certain molybdenum thickness threshold on the interface morphology and, thus, investigate the origins of the reflectivity drops that are shown in Fig. 4.14.

For that purpose, only for selected samples in the vicinity of the presumed crystallization threshold in both sets, as well as far away from that molybdenum thickness

range, the diffuse scattering maps analogous to the previous section were measured. The respective samples are marked with open circles in Fig. 4.13b. In both cases, scattering maps were taken from the samples with lowest and highest Mo layer thickness, respectively, in addition to maps taken from the samples with Mo thicknesses right before, at and right after the presumed crystallization threshold. Table 5.2 lists the reconstructed molybdenum thicknesses corresponding to these samples.

| nominal $d_{\text{Mo}} / \text{nm}$ | reconstructed $d_{\text{Mo}} / \text{nm}$ (unpolished) | reconstructed $d_{\text{Mo}} / \text{nm}$ (polished) |
|--|---|---|
| 1.70 | 1.81($-0.12/+0.24$) | 1.77($-0.22/+0.19$) |
| 1.85 | - | 1.91($-0.12/+0.17$) |
| 2.00 | - | 2.29($-0.28/+0.13$) |
| 2.15 | 2.31($-0.22/+0.21$) | - |
| 2.30 | 2.43($-0.09/+0.16$) | 2.60($-0.12/+0.14$) |
| 2.45 | 2.68($-0.13/+0.16$) | - |
| 2.60 | - | - |
| 2.75 | - | - |
| 2.90 | 3.22($-0.13/+0.11$) | - |
| 3.05 | - | 3.47($-0.19/+0.13$) |

Table 5.2 | List of the reconstructed molybdenum layer thicknesses in the selected samples in both sets investigated with the diffuse scattering analysis in relation to the nominal thickness.

All selected samples were measured in the rocking scan geometry with an opening angle of $\Delta\Theta = 30^\circ$. This is analogous to the measurement of the Mo/B₄C/Si/C sample shown in Fig. 5.4c. In that geometry, a large off-specular increase due to the Kiessig-like peaks was observed. Due to that enhancement, the measured intensity is stronger and further away from the detection threshold of the photo diode. However, as shown above, any other geometry would be equivalently applicable. As discussed in the previous section, it is sufficient to measure only one half space of the maps shown there as the PSD only depends on the absolute value of q_x by the assumption of isotropic roughness in all directions lateral to the interfaces. Thus, the interface morphology may be reconstructed based on this smaller data set reducing the experimental effort. The resulting maps are shown in the reciprocal space representation for both sets in comparison in Fig. 5.14. The maps in Fig. 5.14a show the scattering distribution from the unpolished samples marked with the fitted Mo layer thickness as listed in table 5.2. The polished samples are shown in Fig. 5.14b.

A very prominent observation in both sets, is that one sample in each series shows significantly stronger overall scattering than the others. In addition, both sets show distinctly different scattering distributions clearly differentiating the polished from the unpolished samples. In the case of the polished samples, significantly less scattering can be observed for higher spatial frequencies, whereas more intensity is measured for smaller frequencies. A recognizable characteristic of the off-specular scattering intensity is the observation of a downward tilted Bragg sheet in case of the unpolished samples, which is in contrast to the rocking scan map of the Mo/B₄C/Si/C sample from the beginning of this chapter. This is due to a non-orthogonal roughness correlation throughout the stack with respect to the surface and interfaces first observed by Gullikson and Stearns [50]. We have discussed the theoretical aspects of this effect in Sec. 2.4, but shall investigate this behavior for the specific set of samples studied here.

The downward tilt of the Bragg sheet is clearly observed for all samples in the unpolished series with a similar direction. All samples were measured along the same

Chap
4.2.3
table
4.6

then ?

(un)polished

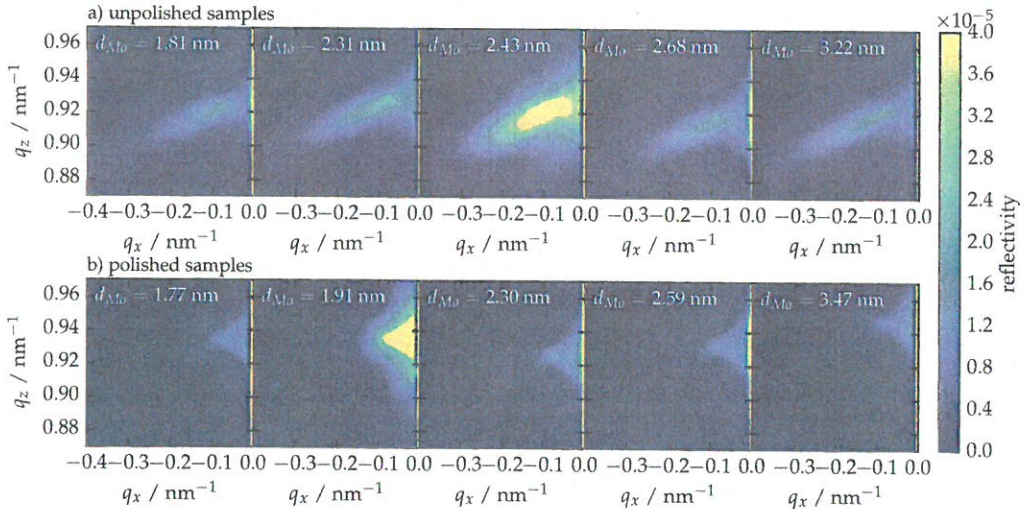


Figure 5.14 | Measured diffuse scattering distributions in reciprocal space representation shown on linear false-color scale. The selected unpolished samples are shown in a) with increasing Mo layer thickness d_{Mo} . The selected samples for the polished set are shown in b) also in order of increasing Mo thickness d_{Mo} . The samples with strongest scattering are shown in larger detail in Fig. 5.16. The diffuse scattering was measured by keeping the detector angle with respect to the incoming beam fixed at $\Delta\Theta = 30^\circ$, while the sample was tilted from an AOI of $\alpha_i = 15^\circ$ to $\alpha_i = 38^\circ$ with a step size $\Delta\alpha_i = 0.5^\circ$. At each angular position, a wavelength scan from $\lambda = 12.35$ nm to $\lambda = 14.0$ nm in steps of $\Delta\lambda = 0.01$ nm was performed to map the diffuse scattering distribution.

nominal x axis, i.e. along the same direction with respect to their mounting orientation during the deposition process. Due to in-plane measurement of the diffuse scattering, the non-orthogonal roughness correlation angle β can only be evaluated along the projection of its directional vector onto the x - z -plane. However, the vertical correlation direction vector may not necessarily lie in that plane. To verify this property, we shall investigate the corresponding diffuse scattering distribution from the strongest scattering sample with $d_{Mo} = 2.43$ nm by rotating it by 90° around its surface normal onto the sample holder and repeat the mapping of reciprocal space. Fig. 5.15 shows the comparison of the map obtained earlier with the map from the rotated sample. The tilt direction is clearly different for the map of the rotated sample, where we obtain a similarly horizontal Bragg sheet as for the Mo/B₄C/Si/C sample in Sec. 5.1. Based on the evaluation of the tilt angle in both maps, it is possible to deduce the direction and total angle β of the roughness correlation direction with respect to the surface normal and the orientation directions of the sample during the measurement. This angle is given by the two orthogonally measured Bragg sheet tilt angles β^0 and β^{90} through

$$\tan^2(\beta) = \tan^2(\beta^0) + \tan^2(\beta^{90}). \quad (5.3)$$

These two independent measurements can be additionally used to verify the results of the reconstruction. We shall thus perform the analysis described in Sec. 5.1 and deduce the PSD parameters including the vertical correlation length as well as the non-orthogonal correlation direction for this sample in particular. For all other measured samples we proceeded in the same way, where here only the in-planar Bragg sheet tilt angle is determined.

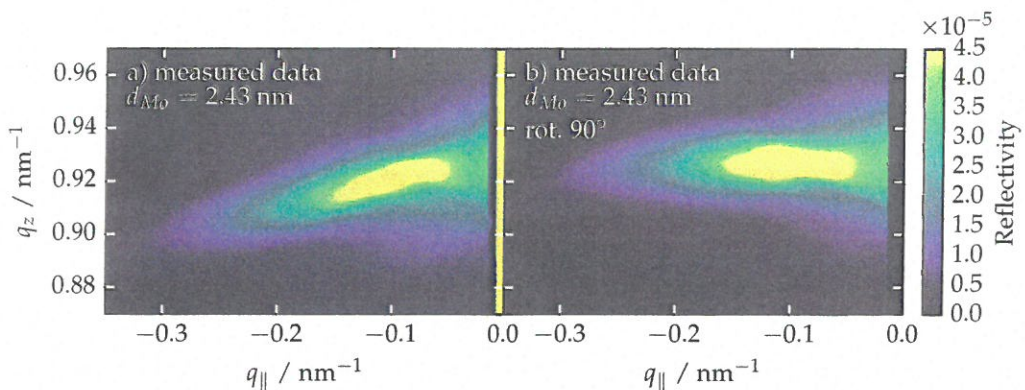


Figure 5.15 | Direct comparison of the measured reciprocal space maps with the DWBA calculation resulting from the parameters obtained with the MCMC optimization procedure (see text). a) shows the maps of the unpolished sample with strongest diffuse scattering. Similarly, b) shows the maps of the polished sample at the respective presumed crystallization threshold with strongest scattering.

5.2.1 Reconstruction of the Interface Morphology

The theoretical analysis was performed based on the method described in the first part of this chapter. Instead of applying the PSO method to reconstruct the parameters characterizing the interface morphology, the MCMC procedure was applied to obtain the optimized parameter values and their confidence intervals. The basic principle is identical to that used in chapter 4 and relies on the minimization functional stated in Eq. (5.2), which enters the likelihood according to the definition in Eq. (4.4). This method is computationally more challenging than applying only the PSO procedure, but becomes possible with the smaller number of periods ($N = 50$) for the samples investigated here, since the effort scales with the order of $O(N^2)$. As starting values, the walkers for the MCMC algorithm were distributed randomly across the parameter space given by the limits listed in table 5.1 with the exception of the Hurst parameter. The latter is limited between 0.8 and 1.0, where the upper limit is the intrinsic theoretical limit representing Gaussian type roughness. The measurements conducted here only allow a limited access to the Hurst parameter, as it is determined by the asymptotic behavior of the PSD towards higher lateral roughness frequencies. For that spacial frequency range, however, no data exists as the vertical correlation of roughness is reduced and the detector threshold is reached so no asymptotic data can be recorded. Others [88] have observed Hurst values in that range for similar samples with values close to the case of Gaussian roughness. The results for the Mo/B₄C/Si/C sample shown in Fig. 5.12 are in good agreement with these findings resulting in a Hurst factor of $H = 1.0$. There, an overall higher in-plane correlation length ($\xi_{||}$) compared to the unpolished samples here, allows a better determination of the asymptotic behavior of the PSD. Due to these results, we analyze the samples from both sets by fixing the Hurst parameter to $H = 1.0$, i.e. by applying a roughness model for Gaussian roughness only. However, in the determination of the confidence intervals, the range from $H = 0.8$ to $H = 1.0$ was considered to reflect this uncertainty in the determination of the parameters.

The results of the ideal model for each sample system entering the DWBA calculation were obtained from the analysis in Sec. 4.2.3. The optimization was conducted by applying the MCMC method with respect to the vertical correlation length ξ_{\perp} in the vertical correlation function $c(q_{||})$, the tilt angle β and all PSD parameters in $C(q_{||})$. For

the two samples, the maps with the strongest scattering from each set are shown in comparison to the best model DWBA calculation (Fig 5.16) found this way. The resulting

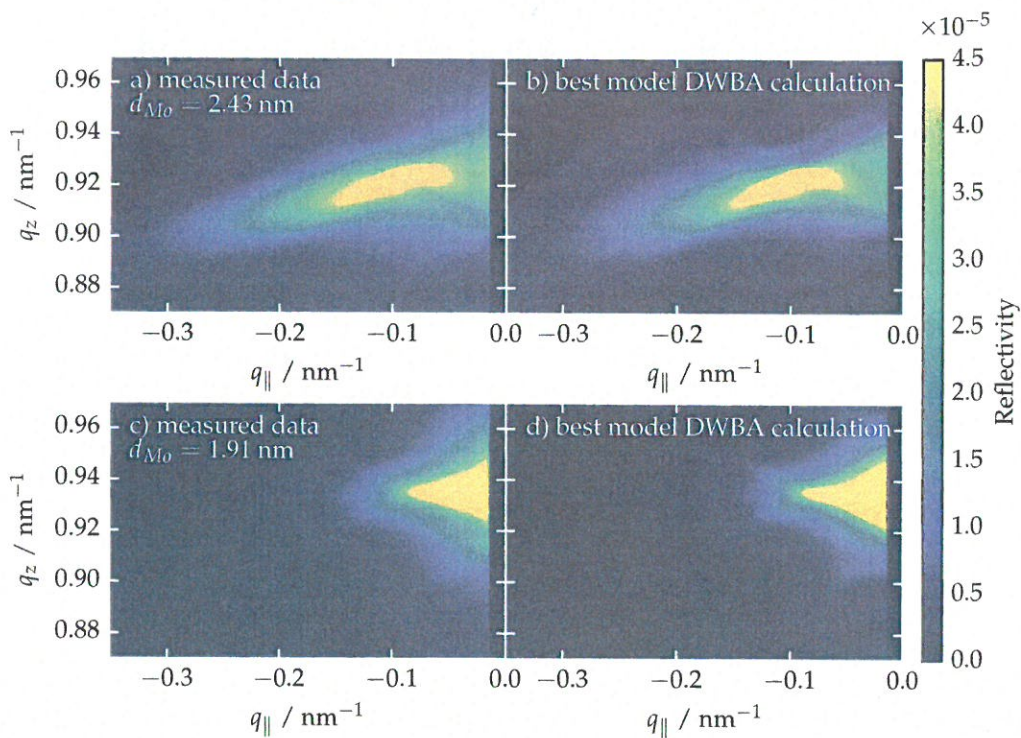


Figure 5.16 | Direct comparison of the measured reciprocal space maps with the DWBA calculation resulting from the parameters obtained with the MCMC optimization procedure (see text). a) shows the maps of the unpolished sample with strongest diffuse scattering. Similarly, b) shows the maps of the polished sample at the respective presumed crystallization threshold with strongest scattering.

maps from the polished and unpolished samples show very good agreement with the theoretical calculation, including the tilted Bragg sheet observed for the unpolished sample. All parameter values obtained from the MCMC optimization procedure are compiled in Table 5.3.

The verification measurement of the rotated sample appears in the row below the respective sample and shows very good agreement with the original measurement. The only exception is the vertical correlation parameter ξ_{\perp} , which is lower in case of the rotated sample. This is due to a truncation of the scattering intensity to higher values of $|q_x|$, because of the absorption due to the Si L₂-edge. From the two measurements, a total non-orthogonal tilt angle of the vertical roughness correlation of $\beta = (5.70 \pm 0.06)^\circ$ is obtained by applying Eq. (5.3). This clearly indicates an anisotropy of the deposition process, which is likely due to non-central mounting of the sample on the sample holder during fabrication. For both sample sets a significant increase of roughness can be observed at the crystallization threshold, which coincides with the lowest reflectance for that sample in each set. Interestingly, the roughness returns to the previous value for further increasing Mo layer thicknesses. This indicates, that the roughening due to the formation of nanocrystallites at the threshold is compensated for even larger thicknesses. We also observe a restored peak reflectance in that case. For the polished samples, the formation of crystallites can be observed with similar effects, but at lower Mo layer thickness with overall significantly lower root mean square roughness values. It should

Table 5.3 | Results for the DWBA model parameters with the respective confidence intervals for both sample sets.

| nom. Mo thickness / nm (fitted Mo thickness / nm) | σ_r / nm | ξ_{\parallel} / nm | ξ_{\perp} / nm $^{-1}$ | β / ° |
|--|---------------------------|-------------------------|----------------------------|-------------------------|
| Unpolished samples | | | | |
| 1.70 (1.81[−0.12/+0.24]) | $0.227^{+0.010}_{-0.003}$ | $3.14^{+0.45}_{-0.06}$ | $3.69^{+0.15}_{-0.16}$ | $-4.62^{+0.05}_{-0.06}$ |
| 2.15 (2.31[−0.22/+0.21]) | $0.232^{+0.009}_{-0.002}$ | $3.72^{+0.44}_{-0.05}$ | $4.88^{+0.17}_{-0.18}$ | $-5.02^{+0.04}_{-0.04}$ |
| 2.30 (2.43[−0.09/+0.16]) | $0.329^{+0.009}_{-0.003}$ | $4.51^{+0.45}_{-0.06}$ | $4.44^{+0.17}_{-0.17}$ | $-5.67^{+0.05}_{-0.06}$ |
| verification 90° | $0.317^{+0.011}_{-0.004}$ | $4.56^{+0.48}_{-0.10}$ | $3.62^{+0.18}_{-0.19}$ | $+0.55^{+0.07}_{-0.07}$ |
| 2.45 (2.68[−0.13/+0.16]) | $0.211^{+0.009}_{-0.003}$ | $3.61^{+0.46}_{-0.06}$ | $3.80^{+0.15}_{-0.16}$ | $-5.06^{+0.06}_{-0.06}$ |
| 2.90 (3.22[−0.13/+0.11]) | $0.243^{+0.009}_{-0.002}$ | $2.89^{+0.43}_{-0.03}$ | $5.72^{+0.14}_{-0.17}$ | $-5.06^{+0.03}_{-0.03}$ |
| Polished samples | | | | |
| 1.70 (1.77[−0.22/+0.19]) | $0.129^{+0.009}_{-0.002}$ | $7.05^{+0.55}_{-0.23}$ | $0.53^{+0.03}_{-0.02}$ | $-1.19^{+0.28}_{-0.28}$ |
| 1.85 (1.91[−0.12/+0.17]) | $0.195^{+0.008}_{-0.002}$ | $10.66^{+0.56}_{-0.19}$ | $0.76^{+0.04}_{-0.04}$ | $-1.50^{+0.25}_{-0.26}$ |
| 2.00 (2.29[−0.28/+0.13]) | $0.105^{+0.005}_{-0.001}$ | $8.95^{+0.52}_{-0.13}$ | $0.76^{+0.03}_{-0.03}$ | $-2.28^{+0.16}_{-0.14}$ |
| 2.30 (2.60[−0.12/+0.14]) | $0.106^{+0.006}_{-0.001}$ | $8.22^{+0.52}_{-0.17}$ | $0.86^{+0.04}_{-0.04}$ | $-2.90^{+0.16}_{-0.07}$ |
| 3.05 (3.47[−0.19/+0.13]) | $0.088^{+0.005}_{-0.001}$ | $10.29^{+0.58}_{-0.19}$ | $1.47^{+0.13}_{-0.11}$ | $-1.62^{+0.16}_{-0.16}$ |

be noted, that the strong roughness increase is only observed for one of the samples in each set, despite that a reduced peak reflectance is seen for two samples out of each set that were associated with the crystallization threshold in Fig. 4.14. In both cases, only the sample with the thicker molybdenum layer of the two shows stronger roughness, which we shall discuss in the following subsection. Another clear difference between the polished and unpolished sets, is the large gap between the vertical correlation factors that is observed. As is to be expected, the polishing process largely reduces the roughness correlation between different interfaces. In the case of unpolished growth, almost the entire stack is correlated for the observable spatial frequencies. The large values for the in-planar correlation length for the polished samples are also a direct result of the polishing process.

5.2.2 Discussion of the Results

Finally, we shall interpret the results and relate them to the findings made in Sec. 4.2. To illustrate the relation between the peak reflectance of each sample and the r.m.s. roughness reconstructed here, Fig. 5.17 shows these parameters in comparison with each other. In addition, the Nérot-Croce parameter from the specular reflectance analysis is included through its confidence interval.

The reconstructed roughness values shown in the figure have the expected increase at the presumed crystallization threshold. We also observed for both sample sets a simultaneous jump at in the total period thickness D and the molybdenum layer thickness around $d_{Mo} = 2.5$ nm for the unpolished samples and $d_{Mo} = 2.2$ nm for the polished

Fig 4.13 b

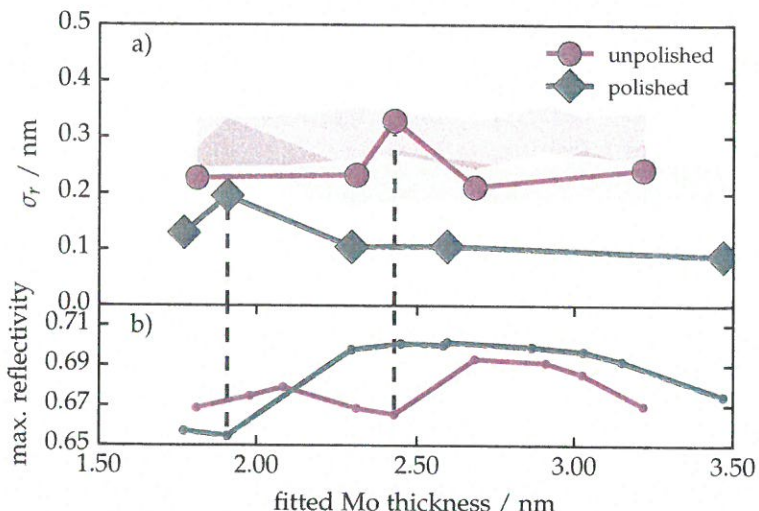


Figure 5.17 | a) Root mean square roughness results from the analysis of the diffuse scattering for the two sample sets together with the full confidence intervals of the Névot-Croce damping factor as obtained from the analysis in Sec. 4.2. In each set, an increase of roughness is observed at the crystallization threshold. For comparison, the max peak reflectance for each sample set is shown in b). The increase in roughness clearly correlates with a significant dip in the peak reflectance as indicated by the dashed vertical lines.

samples. The evaluation of the diffuse scatter revealed increased roughness throughout the multilayer stack for the samples just at the thickness jump. In comparison to the suspected trend of the peak reflectance with d_{Mo} we observed two samples with lower reflectance in both sets, one exactly at the position of this increased scatter and the other sample with nominally 0.15 nm lower d_{Mo} . At least for the unpolished samples, this higher roughness is not observed from evaluating the specular reflectance alone, where the reflectance is diminished by the combined effects of roughness, interdiffusion and compound formation, which is represented by an effective σ -value in the Névot-Croce factor. For the polished samples, the enhanced scatter is also observed in the total Névot-Croce damping factor. In the latter system, the magnitude of the dip, however, is also significantly higher for the two respective samples compared to the rest of the set than for the unpolished samples, which may explain that an increase in the damping factor is less pronounced. The roughness amplitudes as derived from the diffuse scatter, however, have much smaller values. The comparison of the Névot-Croce parameters and the roughness values reveals, that the polishing successfully reduced the roughness contribution to the overall damping factor. It should be noted, that the Névot-Croce parameters confidence intervals have reduced less than the roughness σ_r , compared to the series of unpolished samples. This shows, that the remaining interface distortions through compound formation and intermixing are largely responsible for the gap between theoretically possible reflectance and actual measured values for the polished set.

The interpretation of these findings is in line with the observation of the formation of crystallites in the molybdenum layer at around 2 nm thickness reported by Bajt et al. [7]. Particularly, we assign the threshold to the lower thickness where the reflectance first drops without an observation of increased roughness by diffuse scatter. This is explained (analog to [7]) by the crystallization process starting with increased interdiffusion and small seeds corresponding to a short correlation length, yielding high spacial frequency roughness, not correlated throughout the stack. The corresponding scatter is thus not

resonantly enhanced. Without the enhancement, it is below the detection threshold of our experiment. With increasing crystallites, the diffuse scatter becomes observable at slightly higher molybdenum thickness. Note that for the unpolished sample, the threshold coincides with the point where the ideal Mo-to-Si ratio should yield the highest reflectance in agreement with the findings in [7] and the theoretical calculations shown in Fig. 4.14. For the polished samples, this threshold is shifted to thinner molybdenum layers around $d_{\text{Mo}} = 1.77(-0.22 / +0.19)$ nm. This is beneficial for the peak reflectance, which is higher at the optimum ratio, than for the unpolished set. In both cases, a smoothening occurs for even larger molybdenum thickness, restoring the roughness to its value below the threshold. The evaluation of the diffuse scatter shows an overall lower roughness for the polished samples and, particularly, a destruction of vertical roughness correlation throughout the stack and an increase of the in-planar correlation length, as intended by the polishing.

Finally, we note that the based on the analysis methods introduced in Sec. 4.2 and the diffuse scatter analysis explained in beginning of this chapter is is possible to consistently determine the molybdenum layer thickness and the average power spectral density roughness for the interfaces throughout the full multilayer stack. The application of these methods to Mo/Si multilayer samples with varying molybdenum thickness with/without polishing confirmed previous findings on the onset of molybdenum crystallization in the literature. The results presented in Sec. 4.2 and the analysis of the diffuse scatter discussed here are published together in A. Haase, V. Soltwisch, S. Braun, C. Laubis and F. Scholze: 'Interface Morphology of Mo/Si Multilayer Systems with Varying Mo Layer Thickness Studied by EUV Diffuse Scattering'. In: *Optics Express* (2017).

5.3 Roughness and Intermixing in Cr/Sc Multilayers

In Sec. 4.3, we have demonstrated the analysis of Cr/Sc multilayer mirrors with sub-nanometer layer thicknesses. A more complex model was required to reconstruct the structural parameters unambiguously. The combination of several experiments conducted, could indeed provide a unequivocal solution to most of the parameters shown in table 4.9, with the results and their confidence intervals listed in table 4.11 and illustrated in Fig. 4.29. However, as for the Mo/Si systems investigated in this thesis, the methods applied in Ch 4 do not yield a possibility to distinguish roughness from intermixing. Even though, the spatially resolved methods such as XRF did in combination yield the interface profile asymmetry, a correlation between the intermixing parameter η and the r.m.s. roughness parameter σ_r remains, as seen in Fig. 5.18. *doppelt*

Based on the analysis of the diffuse scatter, as we have shown above, that distinction becomes possible. We finalize this chapter with the analysis of the Cr/Sc sample system studied in Sec. 4.3 and complete the characterization with respect to that parameter correlation. For that purpose, we have measured the diffuse scattering intensity from the Cr/Sc sample similarly to the Mo/Si sample systems above in a rocking scan geometry. As the theoretical model for the DWBA calculation, we applied the gradual interface model as defined in the previous chapter with the optimal parameters listed in table 4.11 for the combination of all analytic experiments conducted there.

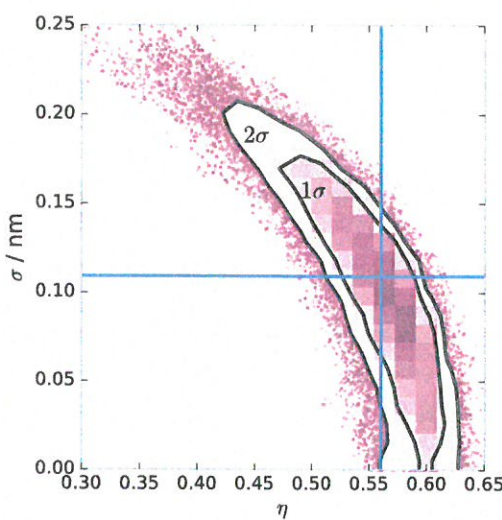
The reciprocal space map was taken at an opening angle of $\Delta\Theta = 3^\circ$, where the specular reflectance condition corresponds to the situation where the EUV reflectivity was evaluated in the previous chapter. This is necessary for this particular sample system

*da r ykell
W. ?
→ Talk
5.3
Fig.
S42
oh,*

Wähly.

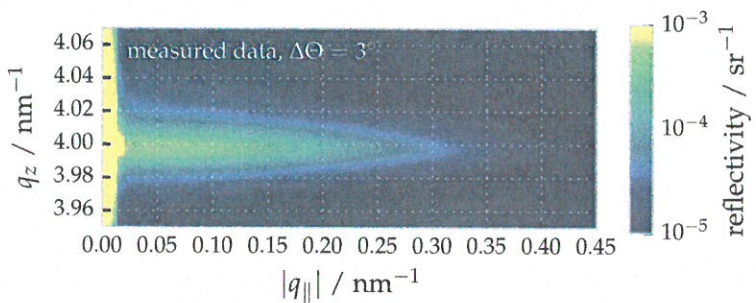
4.28

Figure 5.18 | Correlation of the projected χ^2 surface onto the parameter pair (η, σ_r) by visualization of the position of the MCMC samples in the reduced parameter space.



to fulfill the Bragg condition without decreasing the wavelength to values below the Sc L-edge, where absorption would eliminate the possibility to diffuse scattering from the multilayer. The measurement results are shown in Fig. 5.19. A clear difference to the

Figure 5.19 | Diffuse scattering measurement in q -space representation and log scale.



maps in case of Mo/Si samples is the lack of Kiessig-like peaks and a similar triangular shaped intensity distribution due to the Bragg-like peak. Here, rather the expectation issued at the beginning of the chapter of the observation of a well formed Bragg sheet is met. The reasons behind this different behavior are the fundamental differences with respect to the quality as a mirror of the Cr/Sc system compared to the Mo/Si system and the different measurement geometry. With a EUV peak reflectance of only about 15%, only approximately 27% of the maximum theoretical reflectivity is attained. In the previous chapter, it was found that the gradually shaped interfaces regions and intermixing of the sub-nanometer thick layers play a fundamental role in diminishing the reflectivity. This, however, does also crucially reduce the impact of multiple dynamic reflections, which were found to have a strong impact on the measured diffuse scatter intensity for the Mo/Si multilayer systems investigated above. In addition, this causes significantly higher penetration depth allowing more layers to contribute to the diffuse scatter, even if the Bragg condition is fulfilled for both the incidence and exit angles. Apart from the general lack of dynamic effects due to bad reflectivity at the interfaces, the non-appearance of Kiessig-like peaks is also related to the rocking scan geometry with a significantly smaller opening angle. In the comparison of geometries done at the beginning of this chapter in Fig. 5.7, we have shown that the resonance conditions move to higher absolute values of $q_{||}$, if the opening angle is reduced. Thus, no peaks are to be

?

for Sc/Si

expected in the accessible range for the scan geometry chosen here.

5.3.1 Estimation of the Vertical Roughness Correlation and the PSD

The sample investigated here is represented by the gradual interface model introduced in Sec. 4.2 above. With total number of $N = 400$ bilayers and subsequent subdivision in sublayers, a substantial increase of interfaces has to be considered for the DWBA analysis as compared to the Mo/Si systems. As pointed out above, the computation cost growth quadratically with the order $O(N^2)$ and thus renders the MCMC method very unpractical for this particular system. However, in order to deduct an estimate of the PSD and the vertical roughness correlation, we shall apply the approach introduced in Sec. 5.1 at the beginning of the chapter by analyzing only selected cuts of the map to obtain the relevant parameters. The best PSD model parameters are then obtained by analyzing a horizontal cut of the Bragg sheet divided by the multilayer enhancement factor. The two cut positions are shown in Fig. 5.20 as dashed lines in both, the measured maps and the best model DWBA calculation that was obtained with this approach. The

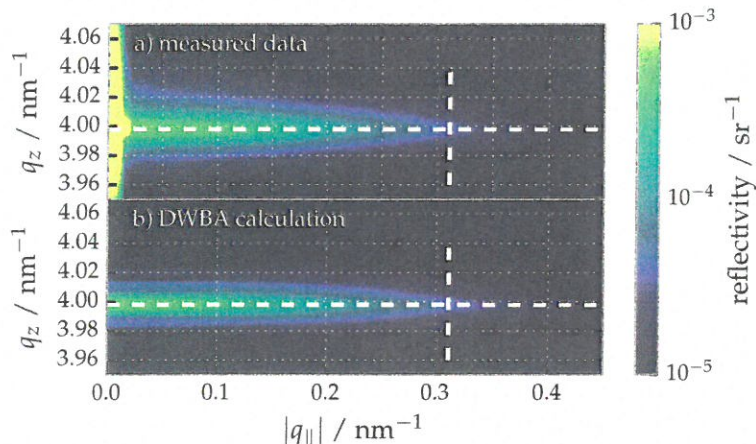


Figure 5.20 | a) Diffuse scattering measurement in q -space representation and log scale. b) DWBA calculation of the optimal PSD model based on the gradual interface model with the multilayer parameters for the combined analysis listed in Table 4.11.

comparison shows a good agreement of the model with the measured data. The data and the simulation results at the vertical cut position are shown in detail in Fig. 5.21. The

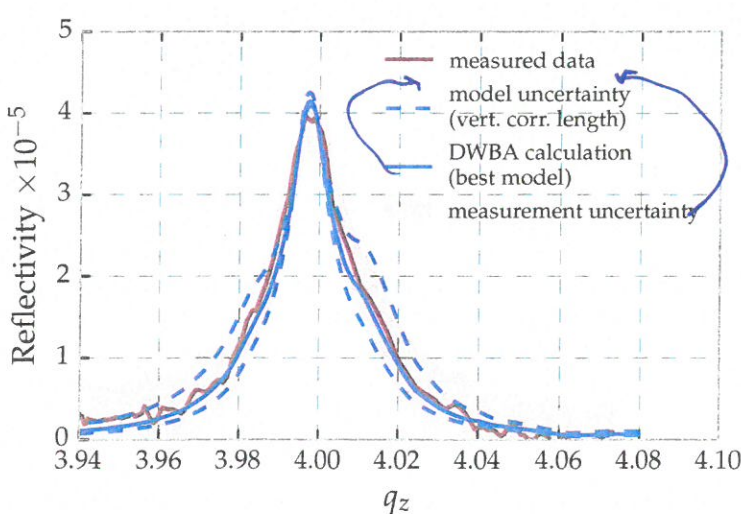
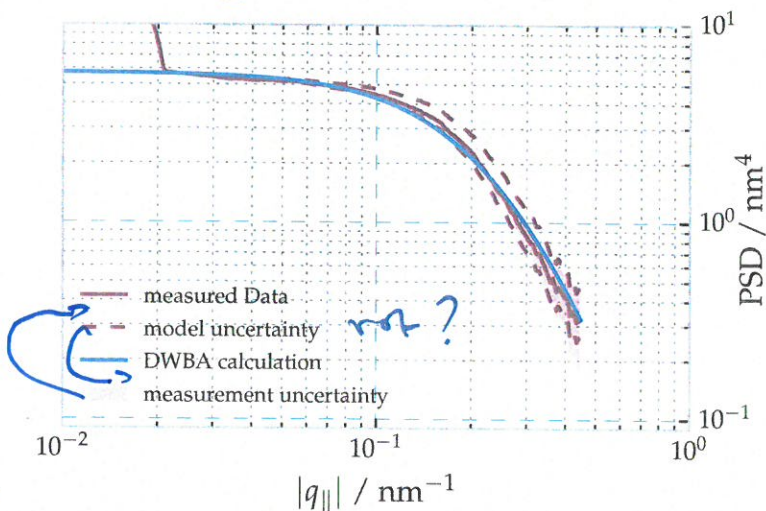


Figure 5.21 | Measured data and calculations at the vertical cut indicated by the vertical white dashed line in Fig. 5.20. The blue dashed lines show two limiting cases for the value of the vertical correlation length. The result is a model uncertainty in the PSD.

leads to
the

solid red line represents the measured data extracted at the aforementioned vertical cut position. The best model result was obtained using the PSO algorithm and is shown as solid blue line providing a good match with the data. The measurement uncertainty is indicated through the red shaded area. Due to the very high computational cost of the MCMC procedure mentioned above, we have instead calculated two limiting cases of the vertical correlation to assess the confidence interval for that parameter. The results of that calculation are shown as dashed blue lines framing the measurement uncertainty at the position of the peak. This parameter enters the calculation of the multilayer enhancement factor marked in Eq. (5.1) and thus affects the absolute values of the PSD extracted from the horizontal cut by dividing through that term. It thus introduces a numerical or model uncertainty to the deduction of the PSD. Proceeding from here, we have evaluated the measured PSD. To deduct the effective power spectral density, we have taken the cut along the Bragg sheet as indicated by the horizontal white dashed lines in the reciprocal space maps. We divided the extracted scattering intensity by the multilayer enhancement factor, leaving the contribution of the effective PSD $C(q_{\parallel})$ to the diffuse scattering. Again, the two limiting cases are shown as red dashed curves in Fig. 5.22 including the PSD deduced from the best model value for ζ_{\perp} as a solid red curve. The r.m.s. roughness,

Figure 5.22 | Comparison of the extracted effective PSDs from the diffuse scattering measurement. The uncertainty interval for the extracted power spectral density is shown by the two dashed PSD profiles (see main text).



which we seek to determine to solve the correlation problem illustrated in Fig. 5.18 above, is given by the two-dimensional integral of the PSD as

$$\sigma_r = \frac{1}{2\pi} \sqrt{\int_0^\infty q_{\parallel} C(q_{\parallel}) dq_{\parallel}}. \quad (5.4)$$

The uncertainty of the PSD due to the vertical correlation leads to an uncertainty in the r.m.s. roughness when evaluating the integral. Due to the limited q_{\parallel} range where measurements can be taken, we have fitted the PSD model of Eq. (2.44) to the resulting data by applying the PSO method based on the parameter limits shown in table 5.1. The additional uncertainty introduced through the model estimate causes a systematic error of the PSD extraction and confidence intervals for the parameters were determined by separately fitting the resulting alternative PSDs. The tilt angle beta was fixed to $\beta = 0^\circ$ in this analysis, since no non-orthogonal roughness correlation was determined by comparison of vertical cuts at different q_{\parallel} positions in the map at this sample orientation. After that, the integration over the full q_{\parallel} range was performed for the best model. The

↓
Show;

Bragg sheet
in Fig. 5.29

| Parameter | Best model values | Confidence interval |
|----------------------------------|-------------------|---------------------|
| σ_r / nm | 0.17 | (-0.01 / + 0.02) |
| ξ_{\parallel} / nm | 3.93 | (-0.42 / + 0.33) |
| ξ_{\perp} / nm ⁻¹ | 10.5 | (-3.5 / + 3.5) |
| H | 1.0 | (-0.03 / + 0.0) |
| β / ° | 0.0 | - |

Table 5.4 | Best model parameters and confidence intervals of the PSD as a result of the diffuse scattering analysis for the gradual Cr/Sc system.

deviation of the integration for the PSD model fit and the data in the available range were negligible. The best model results for the vertical replication factor and the power spectral density are given in Table 5.4, together with their estimated uncertainties.

5.3.2 Results and Conclusions

In Sec. 4.3, we have demonstrated a robust method to characterize ultra-thin multilayer systems with subnanometer layer thicknesses unambiguously. Layer thicknesses in the subnanometer region are necessary for near-normal incidence reflective mirrors in the water window spectral range. However, they come with the cost of increasing susceptibility to disturbances in the interfaces at the layer boundaries. This limits the achievable reflectance to values well below the theoretical threshold. The main mechanisms for diminished reflectance are interdiffusion and roughness. With these effects ranging on the order of the layer thickness, models based on binary layer stacks become inadequate to describe the physical situation. In order to find a proper representation of the multilayer sample, more sophisticated models with an explicit description of the gradual interdiffusion layers become necessary. This inevitably increases the number of parameters to be determined in analytical experiments. Finding an unambiguous solution is challenging and can only be achieved with a combined analysis of several non-destructive techniques.

We performed a rigorous analysis of several experimental methods to determine the model parameters representing one Cr/Sc sample. The optimal set of parameters was determined by applying a particle swarm optimizer in conjunction with a Markov-chain Monte Carlo method to verify the uniqueness of the solution and derive confidence intervals for all parameters in all experiments. Within the verified confidence intervals the MCMC method reveals a remaining correlation between the intermixing parameter η and the roughness factor σ_r , which could not be resolved with the experiments in specular geometry and the fluorescence measurements. In this chapter, we therefore performed a measurement of the off-specular diffuse scattering to distinguish between the roughness and the interdiffusion similarly to the approach used for the Mo/Si systems. The r.m.s. roughness value found with the analysis of the diffuse scattering is identical within its confidence interval to the value obtained from the combined analysis and thus confirms the intermixing and roughness parameters listed in Table 4.11. The results of this analysis further reveal a high degree of roughness correlation throughout the multilayer, which is in agreement with observations made for the unpolished Mo/Si systems and hints at a strong roughness replication during deposition of each layer. It should also be noted here that the interdiffusion width s_d is much larger than the roughness values σ_r . Also none of the layers was found to have the index of refraction of pure Cr or Sc, respectively. This is reflected through the non-vanishing intermixing parameter $\eta > 0$. Thus, it can be concluded that while roughness still exists, intermixing and interdiffusion of the

by reflection

Introduction
??

Anfang
5.3

two materials in these sub-nanometer layer systems are the main cause of diminished reflectance for the Cr/Sc multilayer system studied here.

The findings made in Sec. 4.3 together with the diffuse scattering analysis presented here have been published in A. Haase, S. Bajt, P. Hönicke, V. Soltwisch and F. Scholze: 'Multiparameter characterization of subnanometre Cr/Sc multilayers based on complementary measurements'. en. In: *Journal of Applied Crystallography* **49**.6 (Dec. 2016), pp. 2161–2171. doi: 10.1107/S1600576716015776.

Bewegung von höheren Sprungstellen
und Tälern (Valley) bei
der Diskussion.

Diskussion anfänglich
führen. Verlustlosch! \Rightarrow Diskuss.
Fluss

References

- [1] M. Abramowitz and I. A. Stegun: *Handbook of Mathematical Functions: With Formulas, Graphs, and Mathematical Tables*. en. Courier Corporation, 1964.
- [2] J. Als-Nielsen and D. McMorrow: 'X-rays and their interaction with matter'. en. In: *Elements of Modern X-ray Physics*. John Wiley & Sons, Inc., 2011, pp. 1–28.
- [3] C. Amra: 'From light scattering to the microstructure of thin-filmmultilayers'. In: *Appl. Opt.* **32**.28 (1993), pp. 5481–5491. DOI: 10.1364/AO.32.005481.
- [4] C. Amra: 'Light scattering from multilayer optics. I. Tools of investigation'. In: *J. Opt. Soc. Am. A* **11**.1 (1994), pp. 197–210. DOI: 10.1364/JOSAA.11.000197.
- [5] A. L. Aquila, F. Salmassi, E. M. Gullikson, F. Eriksson and J. Birch: 'Measurements of the optical constants of scandium in the 50–1300eV range'. In: vol. 5538. 2004, pp. 64–71. DOI: 10.1117/12.563615.
- [6] S. Bajt, J. B. Alameda, T. W. Barbee Jr., W. M. Clift, J. A. Folta, B. Kaufmann and E. A. Spiller: 'Improved reflectance and stability of Mo-Si multilayers'. In: *Optical Engineering* **41**.8 (2002), pp. 1797–1804. DOI: 10.1117/1.1489426.
- [7] S. Bajt, D. G. Stearns and P. A. Kearney: 'Investigation of the amorphous-to-crystalline transition in Mo/Si multilayers'. In: *Journal of Applied Physics* **90**.2 (2001), pp. 1017–1025. DOI: <http://dx.doi.org/10.1063/1.1381559>.
- [8] A. Balerna and S. Mobilio: 'Introduction to Synchrotron Radiation'. en. In: *Synchrotron Radiation*. Ed. by S. Mobilio, F. Boscherini and C. Meneghini. DOI: 10.1007/978-3-642-55315-8_1. Springer Berlin Heidelberg, 2015, pp. 3–28.
- [9] J. Barbee Troy W., J. W. Weed, R. B. Hoover, M. J. Allen, J. F. Lindblom, R. H. O'Neal, C. C. Kankelborg, C. E. DeForest, E. S. Paris, A. B. C. Walker II, T. D. Willis, E. S. Gluskin, P. A. Pianetta and P. C. Baker: 'Multi-Spectral Solar Telescope Array II: soft x-ray EUV reflectivity of the multilayer mirrors'. In: *Optical Engineering* **30**.8 (1991), pp. 1067–1075. DOI: 10.1117/12.55917.
- [10] T. W. Barbee, S. Mrowka and M. C. Hettrick: 'Molybdenum-silicon multilayer mirrors for the extreme ultraviolet'. In: *Appl. Opt.* **24**.6 (1985), pp. 883–886. DOI: 10.1364/AO.24.000883.
- [11] G. T. Baumbach, V. Holy, U. Pietsch and M. Gailhanou: 'The influence of specular interface reflection on grazing incidence X-ray diffraction and diffuse scattering from superlattices'. In: *Physica B: Condensed Matter* **198**.1 (1994), pp. 249–252. DOI: 10.1016/0921-4526(94)90172-4.

- [12] G. T. Baumbach, S. Tixier, U. Pietsch and V. Holý: 'Grazing-incidence diffraction from multilayers'. In: *Physical Review B* **51**.23 (1995), pp. 16848–16859. doi: 10.1103/PhysRevB.51.16848.
- [13] M. Bayes and M. Price: 'An Essay towards Solving a Problem in the Doctrine of Chances. By the Late Rev. Mr. Bayes, F. R. S. Communicated by Mr. Price, in a Letter to John Canton, A. M. F. R. S.' en. In: *Philosophical Transactions* **53** (1763), pp. 370–418. doi: 10.1098/rstl.1763.0053.
- [14] B. Beckhoff, A. Gottwald, R. Klein, M. Krumrey, R. Müller, M. Richter, F. Scholze, R. Thornagel and G. Ulm: 'A quarter-century of metrology using synchrotron radiation by PTB in Berlin'. In: *physica status solidi (b)* **246**.7 (2009), pp. 1415–1434. doi: 10.1002/pssb.200945162.
- [15] F. d. Bergevin: 'The Interaction of X-Rays (and Neutrons) with Matter'. en. In: *X-ray and Neutron Reflectivity*. Ed. by J. Daillant and A. Gibaud. Lecture Notes in Physics **770**. DOI: 10.1007/978-3-540-88588-7_1. Springer Berlin Heidelberg, 2009, pp. 1–57.
- [16] R. T. Birge: 'The Calculation of Errors by the Method of Least Squares'. In: *Physical Review* **40**.2 (1932), pp. 207–227. doi: 10.1103/PhysRev.40.207.
- [17] D. K. G. d. Boer, A. J. G. Leenaers and W. W. v. d. Hoogenhof: 'Influence of roughness profile on reflectivity and angle-dependent X-ray fluorescence'. In: *J. Phys. III France* **4**.9 (1994), pp. 1559–1564. doi: 10.1051/jp3:1994222.
- [18] D. K. G. de Boer: 'Glancing-incidence x-ray fluorescence of layered materials'. In: *Physical Review B* **44**.2 (1991), pp. 498–511. doi: 10.1103/PhysRevB.44.498.
- [19] D. K. G. de Boer: 'X-ray reflection and transmission by rough surfaces'. In: *Phys. Rev. B* **51**.8 (1995), pp. 5297–5305. doi: 10.1103/PhysRevB.51.5297.
- [20] D. K. G. de Boer: 'X-ray scattering and x-ray fluorescence from materials with rough interfaces'. In: *Phys. Rev. B* **53**.10 (1996), pp. 6048–6064. doi: 10.1103/PhysRevB.53.6048.
- [21] F. R. Boer: *Cohesion in metals: transition metal alloys*. en. North-Holland, 1988.
- [22] R. Bonifacio, C. Pellegrini and L. M. Narducci: 'Collective instabilities and high-gain regime in a free electron laser'. In: *Optics Communications* **50**.6 (1984), pp. 373–378. doi: 10.1016/0030-4018(84)90105-6.
- [23] M. Born and E. Wolf: *Principles of Optics*. 3rd ed. Cambridge University Press, 1965.
- [24] G. Brandt, J. Eden, R. Fliegauf, A. Gottwald, A. Hoehl, R. Klein, R. Müller, M. Richter, F. Scholze, R. Thornagel, G. Ulm, K. Bürgmann, J. Rahn and G. Wüstefeld: 'The Metrology Light Source – The new dedicated electron storage ring of PTB'. In: *Nuclear Instruments and Methods in Physics Research Section B: Beam Interactions with Materials and Atoms* **258**.2 (2007), pp. 445–452. doi: 10.1016/j.nimb.2007.02.076.
- [25] S. Braun, T. Foltyń, H. Mai, M. Moss and A. Leson: 'Grenzflächen-optimierte Mo/Si Multischichten als Reflektoren für den EUV Spektralbereich. Interface-optimized Mo/Si multilayers as reflectors for the EUV spectral range'. en. In: *Vakuum in Forschung und Praxis* **15**.2 (2003), pp. 76–81. doi: 10.1002/vipr.200390023.
- [26] S. Braun, H. Mai, M. Moss, R. Scholz and A. Leson: 'Mo/Si Multilayers with Different Barrier Layers for Applications as Extreme Ultraviolet Mirrors'. en. In: *Japanese Journal of Applied Physics* **41**.6S (2002), p. 4074. doi: 10.1143/JJAP.41.4074.

- [27] A. Carlisle and G. Dozier: 'An off-the-shelf PSO'. In: *Proceedings of The Workshop On particle Swarm Optimization, Indianapolis, USA.* 2001.
- [28] D. R. Cox and D. V. Hinkley: *Theoretical Statistics*. en. CRC Press, 1979.
- [29] J. W. Criss and L. S. Birks: 'Calculation methods for fluorescent x-ray spectrometry. Empirical coefficients versus fundamental parameters'. In: *Analytical Chemistry* **40**.7 (1968), pp. 1080–1086. doi: 10.1021/ac60263a023.
- [30] Croce, P. and Nérot, L.: 'Étude des couches minces et des surfaces par réflexion rasante, spéculaire ou diffuse, de rayons X'. In: *Rev. Phys. Appl. (Paris)* **11**.1 (1976), pp. 113–125. doi: 10.1051/rphysap:01976001101011300.
- [31] J. Daillant, S. Mora and A. Sentenac: 'Diffuse Scattering'. en. In: *X-ray and Neutron Reflectivity*. Ed. by J. Daillant and A. Gibaud. Lecture Notes in Physics 770. DOI: 10.1007/978-3-540-88588-7_4. Springer Berlin Heidelberg, 2009, pp. 133–182.
- [32] J. Daillant, A. Gibaud, W. Beiglböck, J. Ehlers, K. Hepp, H. A. Weidenmüller, R. Beig, W. Domcke, B.-G. Englert, U. Frisch, P. Hänggi, G. Hasinger, W. Hillebrandt, R. L. Jaffe, W. Janke, H. v. Löhneysen, M. Mangano, J.-M. Raimond, D. Sornette, S. Theisen, W. Weise, J. Zittartz, F. Guinea and D. Vollhardt, eds.: *X-ray and Neutron Reflectivity*. Vol. 770. Lecture Notes in Physics. Berlin, Heidelberg: Springer Berlin Heidelberg, 2009.
- [33] D. A. G. Deacon, L. R. Elias, J. M. J. Madey, G. J. Ramian, H. A. Schwettman and T. I. Smith: 'First Operation of a Free-Electron Laser'. In: *Physical Review Letters* **38**.16 (1977), pp. 892–894. doi: 10.1103/PhysRevLett.38.892.
- [34] Y. S. Derbenev, A. M. Kondratenko and E. L. Saldin: 'On the possibility of using a free electron laser for polarization of electrons in storage rings'. In: *Nuclear Instruments and Methods in Physics Research* **193**.3 (1982), pp. 415–421. doi: 10.1016/0029-554X(82)90233-6.
- [35] B. N. Dev, A. K. Das, S. Dev, D. W. Schubert, M. Stamm and G. Materlik: 'Resonance enhancement of x rays in layered materials: Application to surface enrichment in polymer blends'. In: *Physical Review B* **61**.12 (2000), pp. 8462–8468. doi: 10.1103/PhysRevB.61.8462.
- [36] P. a. M. Dirac: 'A new notation for quantum mechanics'. In: *Mathematical Proceedings of the Cambridge Philosophical Society* **35**.3 (1939), pp. 416–418. doi: 10.1017/S0305004100021162.
- [37] W. T. Elam, B. D. Ravel and J. R. Sieber: 'A new atomic database for X-ray spectroscopic calculations'. In: *Radiation Physics and Chemistry* **63**.2 (2002), pp. 121–128. doi: 10.1016/S0969-806X(01)00227-4.
- [38] J. M. Elson, J. P. Rahn and J. M. Bennett: 'Light scattering from multilayer optics: comparison of theory and experiment'. In: *Appl. Opt.* **19**.5 (1980), pp. 669–679. doi: 10.1364/AO.19.000669.
- [39] J. M. Elson, J. P. Rahn and J. M. Bennett: 'Relationship of the total integrated scattering from multilayer-coated optics to angle of incidence, polarization, correlation length, and roughness cross-correlation properties'. In: *Appl. Opt.* **22**.20 (1983), pp. 3207–3219. doi: 10.1364/AO.22.003207.
- [40] F. Eriksson, G. A. Johansson, H. M. Hertz and J. Birch: 'Enhanced soft x-ray reflectivity of Cr/Sc multilayers by ion-assisted sputter deposition'. In: *Optical Engineering* **41**.11 (2002), pp. 2903–2909. doi: 10.1117/1.1510750.

- [41] F. Eriksson, G. A. Johansson, H. M. Hertz, E. M. Gullikson, U. Kreissig and J. Birch: '14.5% near-normal incidence reflectance of Cr Sc x-ray multilayer mirrors for the water window'. In: *Opt. Lett.* **28**.24 (2003), pp. 2494–2496. DOI: 10.1364/OL.28.002494.
- [42] T. Feigl, S. Yulin, N. Benoit and N. Kaiser: '{EUV} multilayer optics'. In: *Micro-electronic Engineering* **83**.4–9 (2006). Micro- and Nano-Engineering {MNE} 2005 Proceedings of the 31st International Conference on Micro- and Nano-Engineering, pp. 703–706. DOI: <http://dx.doi.org/10.1016/j.mee.2005.12.033>.
- [43] M. Finkenthal, A. P. Zwicker, S. P. Regan, H. W. Moos and D. Stutman: 'Near normal incidence spectroscopy of a Penning ionization discharge in the 110–180 Å range with flat multilayer mirrors'. en. In: *Applied Optics* **29**.24 (1990), p. 3467. DOI: 10.1364/AO.29.003467.
- [44] D. Foreman-Mackey, D. W. Hogg, D. Lang and J. Goodman: 'emcee: The MCMC Hammer'. In: *Publications of the Astronomical Society of the Pacific* **125**.925 (2013). arXiv: 1202.3665, pp. 306–312. DOI: 10.1086/670067.
- [45] C. F. Gauss: *Theoria motus corporum coelestium in sectionibus conicis solem ambientium*. en. 1809.
- [46] N. Ghafoor, F. Eriksson, E. Gullikson, L. Hultman and J. Birch: 'Incorporation of nitrogen in Cr/Sc multilayers giving improved soft x-ray reflectivity'. en. In: *Applied Physics Letters* (2008). DOI: 10.1063/1.2857459.
- [47] S. K. Ghose and B. N. Dev: 'X-ray standing wave and reflectometric characterization of multilayer structures'. In: *Physical Review B* **63**.24 (2001), p. 245409. DOI: 10.1103/PhysRevB.63.245409.
- [48] A. Gibaud and G. Vignaud: 'Specular Reflectivity from Smooth and Rough Surfaces'. en. In: *X-ray and Neutron Reflectivity*. Ed. by J. Daillant and A. Gibaud. Lecture Notes in Physics 770. DOI: 10.1007/978-3-540-88588-7_3. Springer Berlin Heidelberg, 2009, pp. 85–131.
- [49] J. Goodman and J. Weare: 'Ensemble samplers with affine invariance'. en. In: *Communications in Applied Mathematics and Computational Science* **5**.1 (2010), pp. 65–80. DOI: 10.2140/camcos.2010.5.65.
- [50] E. M. Gullikson and D. G. Stearns: 'Asymmetric extreme ultraviolet scattering from sputter-deposited multilayers'. In: *Phys. Rev. B* **59**.20 (1999), pp. 13273–13277. DOI: 10.1103/PhysRevB.59.13273.
- [51] A. Haase, S. Bajt, P. Hönicke, V. Soltwisch and F. Scholze: 'Multiparameter characterization of subnanometre Cr/Sc multilayers based on complementary measurements'. en. In: *Journal of Applied Crystallography* **49**.6 (2016), pp. 2161–2171. DOI: 10.1107/S1600576716015776.
- [52] A. Haase, V. Soltwisch, S. Braun, C. Laubis and F. Scholze: 'Interface Morphology of Mo/Si Multilayer Systems with Varying Mo Layer Thickness Studied by EUV Diffuse Scattering'. In: *Optics Express* (2017).
- [53] A. Haase, V. Soltwisch, C. Laubis and F. Scholze: 'Role of dynamic effects in the characterization of multilayers by means of power spectral density'. In: *Appl. Opt.* **53**.14 (2014), pp. 3019–3027. DOI: 10.1364/AO.53.003019.

- [54] A. Haase, V. Soltwisch, F. Scholze and S. Braun: 'Characterization of Mo/Si mirror interface roughness for different Mo layer thickness using resonant diffuse EUV scattering'. In: *Proc. SPIE*. Vol. 9628. 2015, pp. 962804–962804–7. DOI: 10.1117/12.2191265.
- [55] B. L. Henke, E. M. Gullikson and J. C. Davis: 'X-Ray Interactions: Photoabsorption, Scattering, Transmission, and Reflection at $E = 50\text{--}30,000 \text{ eV}$, $Z = 1\text{--}92$ '. In: *Atomic Data and Nuclear Data Tables* **54**.2 (1993), pp. 181–342. DOI: <http://dx.doi.org/10.1006/adnd.1993.1013>.
- [56] H. M. Hertz, L. Rymell, M. Berglund, G. A. Johansson, T. Wilhein, Y. Y. Platonov and D. M. Broadway: 'Normal-incidence condenser mirror arrangement for compact water-window x-ray microscopy'. In: *Proc. SPIE* **3766** (1999), pp. 247–251. DOI: 10.1117/12.363641.
- [57] M. P. Hobson and J. E. Baldwin: 'Markov-chain Monte Carlo approach to the design of multilayer thin-film optical coatings'. EN. In: *Applied Optics* **43**.13 (2004), pp. 2651–2660. DOI: 10.1364/AO.43.002651.
- [58] V. Holý and T. Baumbach: 'Nonspecular X-ray reflection from rough multilayers'. In: *Phys. Rev. B* **49**.15 (1994), pp. 10668–10676. DOI: 10.1103/PhysRevB.49.10668.
- [59] V. Holý, T. Baumbach and M. Bessiere: 'Interface roughness in surface-sensitive X-ray methods'. en. In: *Journal of Physics D: Applied Physics* **28**.4A (1995), A220. DOI: 10.1088/0022-3727/28/4A/043.
- [60] V. Holý, J. Kuběna, I. Ohlidal, K. Lischka and W. Plotz: 'X-ray reflection from rough layered systems'. In: *Phys. Rev. B* **47**.23 (1993), pp. 15896–15903. DOI: 10.1103/PhysRevB.47.15896.
- [61] X. Jiang, T. H. Metzger and J. Peisl: 'Nonspecular x-ray scattering from the amorphous state in W/C multilayers'. en. In: *Applied Physics Letters* **61**.8 (1992), pp. 904–906. DOI: 10.1063/1.107723.
- [62] J. Kennedy: 'Particle Swarm Optimization'. en. In: *Encyclopedia of Machine Learning*. Ed. by C. Sammut and G. I. Webb. DOI: 10.1007/978-0-387-30164-8_630. Springer US, 2011, pp. 760–766.
- [63] H. Kiessig: 'Interferenz von Röntgenstrahlen an dünnen Schichten'. In: *Annalen der Physik* **402**.7 (1931), pp. 769–788. DOI: 10.1002/andp.19314020702.
- [64] J. Kirz, C. Jacobsen and M. Howells: 'Soft X-ray microscopes and their biological applications'. In: *Quarterly Reviews of Biophysics* **28**.01 (1995), pp. 33–130. DOI: 10.1017/S0033583500003139.
- [65] M. Krumrey: 'Design of a Four-Crystal Monochromator Beamline for Radiometry at BESSY II'. en. In: *Journal of Synchrotron Radiation* **5**.1 (1998), pp. 6–9. DOI: 10.1107/S0909049597011825.
- [66] L. D. Landau and E.M. Lifshitz: *Electrodynamics of Continuous Media. A Course of Theoretical Physics* 8. Oxford, London, New York, Paris: Pergamon Press, 1960.
- [67] H. Legall, G. Blobel, H. Stiel, W. Sandner, C. Seim, P. Takman, D. H. Martz, M. Selin, U. Vogt, H. M. Hertz, D. Esser, H. Sipma, J. Luttmann, M. Höfer, H. D. Hoffmann, S. Yulin, T. Feigl, S. Rehbein, P. Guttmann, G. Schneider, U. Wiesemann, M. Wirtz and W. Diete: 'Compact x-ray microscope for the water window based on a high brightness laser plasma source'. In: *Opt. Express* **20**.16 (2012), pp. 18362–18369. DOI: 10.1364/OE.20.018362.

- [68] A.-M. Legendre: *Nouvelles méthodes pour la détermination des orbites des comètes*. fr. F. Didot, 1805.
- [69] K. Levenberg: 'A method for the solution of certain non-linear problems in least square'. In: *Quarterly of Applied Mathematics* (1944).
- [70] J. R. Levine, J. B. Cohen, Y. W. Chung and P. Georgopoulos: 'Grazing-incidence small-angle X-ray scattering: new tool for studying thin film growth'. In: *Journal of Applied Crystallography* 22.6 (1989), pp. 528–532. doi: 10.1107/S002188988900717X.
- [71] Y. Lim, T. Westerwalbesloh, A. Aschentrup, O. Wehmeyer, G. Haindl, U. Kleineberg and U. Heinzmann: 'Fabrication and characterization of EUV multilayer mirrors optimized for small spectral reflection bandwidth'. In: *Applied Physics A* 72.1 (2001), pp. 121–124. doi: 10.1007/s003390000723.
- [72] H. A. Lorentz: 'The theorem of Poynting concerning the energy in the electromagnetic field and two general propositions concerning the propagation of light'. In: *Amsterdammer Akademie der Wetenschappen* 4 (1896), p. 176.
- [73] J. Lubeck, B. Beckhoff, R. Fliegauf, I. Hofelder, P. Hönicke, M. Müller, B. Polakowski, F. Reinhardt and J. Weser: 'A novel instrument for quantitative nanoanalytics involving complementary X-ray methodologies'. In: *Review of Scientific Instruments* 84.4 (2013), p. 045106. doi: 10.1063/1.4798299.
- [74] D. J. C. MacKay: *Information Theory, Inference and Learning Algorithms*. en. Cambridge University Press, 2003.
- [75] J. M. J. Madey: 'Stimulated Emission of Bremsstrahlung in a Periodic Magnetic Field'. In: *Journal of Applied Physics* 42.5 (1971), pp. 1906–1913. doi: 10.1063/1.1660466.
- [76] D. W. Marquardt: 'An algorithm for least-squares estimation of nonlinear parameters'. In: *Journal of the society for Industrial and Applied Mathematics* 11.2 (1963), pp. 431–441.
- [77] D. S. Martínez-Galarce, I. Walker Arthur B. C., D. B. Gore, C. C. Kankelborg, R. B. Hoover, J. Barbee T. W. and P. F. X. Boerner: 'High resolution imaging with multilayer telescopes: resolution performance of the MSSTA II telescopes'. In: *Optical Engineering* 39.4 (2000), pp. 1063–1079. doi: 10.1117/1.602468.
- [78] P. Mikulík: 'X-ray reflectivity from planar and structured multilayers'. PhD thesis. Thèse de l'Université Joseph Fourier, 1997.
- [79] J. S. Milton and J. C. Arnold: *Introduction to Probability and Statistics: Principles and Applications for Engineering and the Computing Sciences*. 4th. New York, NY, USA: McGraw-Hill, Inc., 2002.
- [80] S. V. Milton, E. Gluskin, N. D. Arnold, C. Benson, W. Berg, S. G. Biedron, M. Borland, Y.-C. Chae, R. J. Dejus, P. K. D. Hartog et al.: 'Exponential Gain and Saturation of a Self-Amplified Spontaneous Emission Free-Electron Laser'. en. In: *Science* 292.5524 (2001), pp. 2037–2041. doi: 10.1126/science.1059955.
- [81] I. H. MUNRO and G. V. MARR: 'CHAPTER 1 - SYNCHROTRON RADIATION SOURCES'. In: *Handbook on Synchrotron Radiation*. Handbook on Synchrotron Radiation. Amsterdam: Elsevier, 1987, pp. 1–20.
- [82] H. Nakajima, H. Fujimori and M. Koiwa: 'Interdiffusion and structural relaxation in Mo/Si multilayer films'. In: *Journal of Applied Physics* 63.4 (1988), pp. 1046–1051. doi: <http://dx.doi.org/10.1063/1.340005>.

- [83] Nérot, L. and Croce, P.: 'Caractérisation des surfaces par réflexion rasante de rayons X. Application à l'étude du polissage de quelques verres silicates'. In: *Rev. Phys. Appl. (Paris)* **15**.3 (1980), pp. 761–779. DOI: 10.1051/rphysap:01980001503076100.
- [84] A. K. Petford-Long, M. B. Stearns, C.-H. Chang, S. R. Nutt, D. G. Stearns, N. M. Ceglio and A. M. Hawryluk: 'High-resolution electron microscopy study of x-ray multilayer structures'. In: *Journal of Applied Physics* **61**.4 (1987), pp. 1422–1428. DOI: <http://dx.doi.org/10.1063/1.338122>.
- [85] U. Pietsch, V. Holý and T. Baumbach: *High-Resolution X-Ray Scattering From Thin Films to Lateral Nanostructures*. Springer, 2004.
- [86] M. Prascioli, A. Haase, F. Scholze, H. N. Chapman and S. Bajt: 'Extended asymmetric-cut multilayer X-ray gratings'. EN. In: *Optics Express* **23**.12 (2015), pp. 15195–15204. DOI: 10.1364/OE.23.015195.
- [87] M. Prascioli, A. F. G. Leontowich, K. R. Beyerlein and S. Bajt: 'Thermal stability studies of short period Sc/Cr and Sc/B₄C/Cr multilayers'. In: *Appl. Opt.* **53**.10 (2014), pp. 2126–2135. DOI: 10.1364/AO.53.002126.
- [88] A. Rack, T. Weitkamp, M. Riotte, D. Grigoriev, T. Rack, L. Helfen, T. Baumbach, R. Dietsch, T. Holz, M. Krämer, F. Siewert, M. Meduňa, P. Cloetens and E. Ziegler: 'Comparative study of multilayers used in monochromators for synchrotron-based coherent hard X-ray imaging'. en. In: *Journal of Synchrotron Radiation* **17**.4 (2010), pp. 496–510. DOI: 10.1107/S0909049510011623.
- [89] S. D. Rasberry and K. F. J. Heinrich: 'Calibration for interelement effects in x-ray fluorescence analysis'. In: *Analytical Chemistry* **46**.1 (1974), pp. 81–89. DOI: 10.1021/ac60337a027.
- [90] R. M. Rousseau: 'Fundamental algorithm between concentration and intensity in XRF analysis 1—theory'. en. In: *X-Ray Spectrometry* **13**.3 (1984), pp. 115–120. DOI: 10.1002/xrs.1300130306.
- [91] N. N. Salashchenko and E. A. Shamov: 'Short-period X-ray multilayers based on Cr/Sc'. In: *Optics Communications* **134**.1–6 (1997), pp. 7–10. DOI: [http://dx.doi.org/10.1016/S0030-4018\(96\)00551-2](http://dx.doi.org/10.1016/S0030-4018(96)00551-2).
- [92] T. Salditt, T. H. Metzger and J. Peisl: 'Kinetic Roughness of Amorphous Multilayers Studied by Diffuse X-Ray Scattering'. In: *Phys. Rev. Lett.* **73**.16 (1994), pp. 2228–2231. DOI: 10.1103/PhysRevLett.73.2228.
- [93] F. Schäfers, H.-C. Mertins, F. Schmolla, I. Packe, N. N. Salashchenko and E. A. Shamov: 'Cr/Sc multilayers for the soft-X-ray range'. In: *Appl. Opt.* **37**.4 (1998), pp. 719–728. DOI: 10.1364/AO.37.000719.
- [94] F. Scholze, J. Tümmler and G. Ulm: 'High-accuracy radiometry in the EUV range at the PTB soft x-ray beamline'. en. In: *Metrologia* **40**.1 (2003), S224. DOI: 10.1088/0026-1394/40/1/352.
- [95] F. Scholze, B. Beckhoff, G. Brandt, R. Fliegauf, A. Gottwald, R. Klein, B. Meyer, U. D. Schwarz, R. Thornagel, J. Tuemmler, K. Vogel, J. Weser and G. Ulm: 'High-accuracy EUV metrology of PTB using synchrotron radiation'. In: *Proc. SPIE*. Vol. 4344. 2001, pp. 402–413. DOI: 10.1117/12.436766.
- [96] S. Schröder, T. Herffurth, H. Blaschke and A. Duparré: 'Angle-resolved scattering: an effective method for characterizing thin-film coatings'. In: *Appl. Opt.* **50**.9 (2011), pp. C164–C171. DOI: 10.1364/AO.50.00C164.

- [97] S. Schröder, D. Unglaub, M. Trost, X. Cheng, J. Zhang and A. Duparré: 'Spectral angle resolved scattering of thin film coatings'. EN. In: *Applied Optics* **53**.4 (2014), A35–A41. DOI: 10.1364/AO.53.000A35.
- [98] J. Schwinger: 'On the Classical Radiation of Accelerated Electrons'. In: *Physical Review* **75**.12 (1949), pp. 1912–1925. DOI: 10.1103/PhysRev.75.1912.
- [99] J. Sherman: 'The theoretical derivation of fluorescent X-ray intensities from mixtures'. In: *Spectrochimica Acta* **7** (1955), pp. 283–306. DOI: 10.1016/0371-1951(55)80041-0.
- [100] T. Shiraiwa and N. Fujino: 'Theoretical Calculation of Fluorescent X-Ray Intensities in Fluorescent X-Ray Spectrochemical Analysis.' en. In: *Japanese Journal of Applied Physics* **5**.10 (1966), p. 886. DOI: 10.1143/JJAP.5.886.
- [101] P. Siffalovic, E. Majkova, L. Chitu, M. Jergel, S. Luby, J. Keckes, G. Maier, A. Timmann, S. V. Roth, T. Tsuru, T. Harada, M. Yamamoto and U. Heinzmann: 'Characterization of Mo/Si soft X-ray multilayer mirrors by grazing-incidence small-angle X-ray scattering'. In: *Vacuum* **84**.1 (2009), pp. 19–25. DOI: <http://dx.doi.org/10.1016/j.vacuum.2009.04.026>.
- [102] S. K. Sinha: 'X-ray diffuse scattering as a probe for thin film and interface structure'. In: *J. Phys. III France* **4**.9 (1994), pp. 1543–1557. DOI: 10.1051/jp3:1994221.
- [103] S. K. Sinha, E. B. Sirota, S. Garoff and H. B. Stanley: 'X-ray and neutron scattering from rough surfaces'. In: *Phys. Rev. B* **38**.4 (1988), pp. 2297–2311. DOI: 10.1103/PhysRevB.38.2297.
- [104] V. Soltwisch, A. Haase, J. Wernecke, J. Probst, M. Schoengen, S. Burger, M. Krumrey and F. Scholze: 'Correlated diffuse x-ray scattering from periodically nanostructured surfaces'. In: *Physical Review B* **94**.3 (2016), p. 035419. DOI: 10.1103/PhysRevB.94.035419.
- [105] V. Soltwisch, A. Fischer, C. Laubis, C. Stadelhoff, F. Scholze and A. Ullrich: 'Polarization resolved measurements with the new EUV ellipsometer of PTB'. In: *Proc. SPIE*. Vol. 9422. 2015, pp. 942213–7. DOI: 10.1117/12.2085798.
- [106] E. Spiller: 'Low-Loss Reflection Coatings Using Absorbing Materials'. In: *Applied Physics Letters* **20**.9 (1972), pp. 365–367. DOI: <http://dx.doi.org/10.1063/1.1654189>.
- [107] E. Spiller, D. Stearns and M. Krumrey: 'Multilayer X-ray mirrors: Interfacial roughness, scattering, and image quality'. In: *Journal of applied physics* **74**.1 (1993), pp. 107–118.
- [108] D. G. Stearns: 'X-ray scattering from interfacial roughness in multilayer structures'. In: *Journal of Applied Physics* **71**.9 (1992), pp. 4286–4298. DOI: 10.1063/1.350810.
- [109] D. G. Stearns, R. S. Rosen and S. P. Vernon: 'Fabrication of high-reflectance Mo-Si multilayer mirrors by planar-magnetron sputtering'. en. In: *Journal of Vacuum Science & Technology A: Vacuum, Surfaces, and Films* **9**.5 (1991), pp. 2662–2669. DOI: 10.1116/1.577221.
- [110] A. C. Thompson and D. Vaughan, eds.: *X-ray Data Booklet*. Second. Lawrence Berkeley National Laboratory, University of California, 2001.
- [111] R. Thornagel, R. Klein and G. Ulm: 'The electron storage ring BESSY II as a primary source standard from the visible to the X-ray range'. en. In: *Metrologia* **38**.5 (2001), p. 385. DOI: 10.1088/0026-1394/38/5/3.

- [112] M. Toyoda, Y. Shitani, M. Yanagihara, T. Ejima, M. Yamamoto and M. Watanabe: 'A Soft-X-Ray Imaging Microscope with a Multilayer-Coated Schwarzschild Objective: Imaging Tests'. en. In: *Japanese Journal of Applied Physics* **39**.Part 1, No. 4A (2000), pp. 1926–1929. DOI: [10.1143/JJAP.39.1926](https://doi.org/10.1143/JJAP.39.1926).
- [113] J. Tummler, H. Blume, G. Brandt, J. Eden, B. Meyer, H. Scherr, F. Scholz, F. Scholze and G. Ulm: 'Characterization of the PTB EUV reflectometry facility for large EUVL optical components'. In: *Proc. SPIE* **5037** (2003), pp. 265–273. DOI: [10.1117/12.482668](https://doi.org/10.1117/12.482668).
- [114] J. Verhoeven, L. Chunguang, E. J. Puik, M. J. van der Wiel and T. P. Huijgen: 'Ion beam modification of Mo?Si multilayer systems for X-ray reflection'. In: *Applied Surface Science* **55.2** (1992), pp. 97–103. DOI: [10.1016/0169-4332\(92\)90099-J](https://doi.org/10.1016/0169-4332(92)90099-J).
- [115] B. Vidal and P. Vincent: 'Metallic multilayers for x rays using classical thin-film theory'. en. In: *Applied Optics* **23.11** (1984), p. 1794. DOI: [10.1364/AO.23.001794](https://doi.org/10.1364/AO.23.001794).
- [116] S. N. Yakunin, I. A. Makhotkin, K. V. Nikolaev, R. W. E. v. d. Kruijs, M. A. Chuev and F. Bijkerk: 'Combined EUV reflectance and X-ray reflectivity data analysis of periodic multilayer structures'. In: *Opt. Express* **22.17** (2014), pp. 20076–20086. DOI: [10.1364/OE.22.020076](https://doi.org/10.1364/OE.22.020076).
- [117] S. A. Yulin, F. Schaefers, T. Feigl and N. Kaiser: 'High-performance Cr/Sc multilayers for the soft x-ray range'. In: *Proc. SPIE* **5193** (2004), pp. 172–176. DOI: [10.1117/12.505688](https://doi.org/10.1117/12.505688).

